J. Fluid Mech. (2025), *vol.* 1024, A47, doi:10.1017/jfm.2025.10892

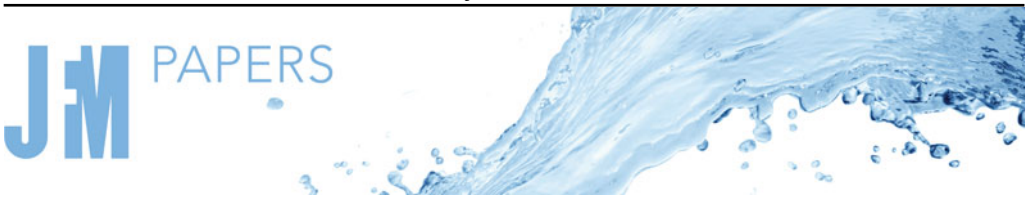

Three-dimensional velocity gradient statistics in a mesoscale convection laboratory experiment

Prafulla P. Shevkar[1], **Roshan J. Samuel**[1], **Christian Cierpka**[1] and **Jörg Schumacher**[1]

[1]Institute of Thermodynamics and Fluid Mechanics, Technische Universität Ilmenau, Postfach 100565, D-98684 Ilmenau, Germany

Corresponding authors: Prafulla P. Shevkar, prafulla-prakash.shevkar@tu-ilmenau.de; Jörg Schumacher, joerg.schumacher@tu-ilmenau.de

(Received 29 May 2025; revised 15 September 2025; accepted 28 October 2025)

We present three-dimensional velocity gradient statistics from turbulent Rayleigh–Bénard convection experiments in a horizontally extended cell of aspect ratio 25, a paradigm for mesoscale convection with its organisation into large-scale patterns. The Rayleigh number Ra ranges from 3.7×10^5 to 4.8×10^6, the Prandtl number Pr from 5 to 7.1. Spatio-temporally resolved volumetric data are reconstructed from moderately dense Lagrangian particle tracking measurements. All nine components of the velocity gradient tensor from the experiments show good agreement with those from direct numerical simulations, both conducted at $Ra = 1 \times 10^6$ and $Pr = 6.6$. As expected, with increasing Ra, the flow in the bulk approaches isotropic conditions in the horizontal plane. The focus of our analysis is on non-Gaussian velocity gradient statistics. We demonstrate that statistical convergence of derivative moments up to the sixth order is achieved. Specifically, we examine the probability density functions (PDFs) of components of the velocity gradient tensor, vorticity components, kinetic energy dissipation and local enstrophy at different heights in the bottom half of the cell. The probability of high-amplitude derivatives increases from the bulk to the bottom plate. A similar trend is observed with increasing Ra at fixed height. Both indicate enhanced small-scale intermittency of the velocity field. We also determine derivative skewness and flatness. The PDFs of the derivatives with respect to the horizontal coordinates are found to be more symmetric than the ones with respect to the vertical coordinate. The conditional statistical analysis of the velocity derivatives with respect to up-/down-welling regions and the rest did not display significant difference, most probably due to the moderate Rayleigh numbers. Furthermore, doubly logarithmic plots of the PDFs of normalised energy dissipation and local enstrophy at all heights show that the left tails follow slopes of 3/2 and 1/2, respectively, in agreement with numerical results. In general, the left tails of the dissipation and local enstrophy distributions show

higher probability values with increasing proximity towards the plate, in comparison with those in the bulk.

Key words: turbulent convection, intermittency, Bénard convection

1. Introduction

Turbulent convection is commonly studied in horizontally extended layers to understand the flow dynamics in the Earth's atmosphere, mantle and oceans, as well as in electronic cooling systems (Incropera 1988; Atkinson & Wu Zhang 1996). In Rayleigh–Bénard (RB) convection, a fluid layer of height H is confined between a heated bottom plate and a cooled top plate, resulting in the formation of convection rolls within the bulk of the cell. Turbulence statistics obtained from these convection experiments offer valuable insights into mesoscale geophysical as well as engineering applications (Alam *et al.* 2025). The term mesoscale convection stems from geo- and astrophysical contexts and denotes there convective turbulence in layers with an intermediate range of extensions ℓ, i.e. scales between $\ell \sim H$ and global scales $\ell \gtrsim L = \Gamma H$, with L the horizontal extension of the layer. Mesoscale convection proceeds in layers with aspect ratios $\Gamma \gg 1$ and is connected with the formation of large-scale patterns, such as granules on the solar surface (Alam *et al.* 2025). Turbulent convection in such extended systems will be investigated here. In fluid turbulence, energy is injected at the largest scales and dissipated at the smallest ones; it is transferred through a broad intermediate range of scales. Therefore, quantifying the rate of kinetic energy dissipation, defined as

$$\epsilon(x_k, t) = 2\nu S_{ij} S_{ij} = \frac{\nu}{2}\left(\frac{\partial u_i}{\partial x_j} + \frac{\partial u_j}{\partial x_i}\right)^2, \tag{1.1}$$

is essential for understanding the energy cascade. Here, ν is the kinematic viscosity of the fluid, u_i the velocity field, and S_{ij} the strain rate tensor. Similarly, it is important to characterise the local enstrophy, defined as

$$\Omega(x_k, t) = \omega_i \omega_i = \frac{1}{2}\left(\frac{\partial u_i}{\partial x_j} - \frac{\partial u_j}{\partial x_i}\right)^2, \tag{1.2}$$

as it quantifies the intensity of vortical structures across scales, where $\omega = \sqrt{\omega_i \omega_i}$ is the magnitude of the vorticity field $\omega_i = \varepsilon_{ijk}\partial u_k/\partial x_j$, with indices $i, j, k = 1, 2, 3$. The symbol ϵ_{ijk} is the anti-symmetric third-rank Levi-Civita tensor. Both dissipation and local enstrophy exhibit strong and localised fluctuations. The latter has even been found to be more intermittent than the former in homogeneous and isotropic turbulence (Chen, Sreenivasan & Nelkin 1997; Chen & Chen 1998; Yeung, Zhai & Sreenivasan 2015). More broadly, such fluctuations in velocity gradients, vorticity components, enstrophy and dissipation are collectively referred to as manifestations of intermittency or the vigour of turbulence. The tails of the probability density functions (PDFs) of velocity gradients are known to exhibit a transition from a Gaussian distribution at low Reynolds numbers, *Re*, to a non-Gaussian, intermittent one at higher *Re* in both homogeneous isotropic turbulence (HIT) and Rayleigh–Bénard convection (RBC) (Schumacher *et al.* 2014). This transition is evident as increasingly wider tails in the PDFs with increasing Reynolds or Rayleigh number in RBC. The Reynolds and Rayleigh numbers are given by

$$Re = \frac{U_{rms} H}{\nu} \quad \text{and} \quad Ra = \frac{g\alpha \Delta T H^3}{\nu\kappa}, \tag{1.3}$$

where g is the acceleration due to gravity, ΔT the temperature difference between the hot and cold plates, H the height of the convection cell, α the thermal expansion coefficient, κ the thermal diffusivity and U_{rms} the root mean square velocity (see also Appendix A).

Furthermore, the transverse component of vorticity, measured using stereoscopic particle image velocimetry (PIV) in RBC experiments with aspect ratio $\Gamma = L/H = 10$ in air, also demonstrates transition from Gaussian to non-Gaussian statistics with respect to velocity derivatives (Valori, Kräuter & Schumacher 2022). Here, L is the horizontal length of the cell, as already discussed above. Ghazijahini & Cierpka (2024) showed for the convection cell that out-of-plane vortices are prominent and their number increases with Ra with additional broader tails for the PDFs of the velocity components. The vigour of turbulence in RBC is also characterised by the strength of the internally generated large-scale circulation (LSC), which is known to strongly depend on the aspect ratio of the convection cell (Niemela *et al.* 2001; Bailon-Cuba, Emran & Schumacher 2010; Wagner & Shishkina 2013; Shevkar, Mohanan & Puthenveettil 2023). The superstructures, which are evident in high-aspect-ratio cells, are essentially horizontal organisations into patterns of the LSC in the bulk. They exhibit stronger fluctuations with increasing Ra (Pandey *et al.* 2018; Moller *et al.* 2022), which serves as a further signature of enhanced intermittency at higher Rayleigh number.

Numerical approaches enable three-dimensional statistical analyses using both velocity and temperature fields over a broad range of Rayleigh numbers (Ra). The Prandtl number Pr is another important control parameter in turbulent convection, where $Pr = \nu/\kappa$. Statistical studies conducted for aspect ratio $\Gamma \sim 1$ and Prandtl number $Pr \sim 1$ are reported in the literature such as in Verzicco & Camussi (2003), Zhang, Zhou & Sun (2017) and Venugopal, De & Mishra (2022). Notably, at the same Grashof number $Gr = Ra/Pr$, a significantly higher flow Reynolds number is observed at $Pr = 0.021$ than at $Pr = 0.7$, indicating more vigorous turbulence at lower Prandtl numbers (Schumacher, Götzfried & Scheel 2015). Performing highly resolved direct numerical simulations (DNS) in turbulent RBC for $Pr = 0.7$ and $Pr = 6$, Scheel, Emran & Schumacher (2013) found that the high-amplitude kinetic energy dissipation and thermal dissipation events and their range of scales decrease with increasing Pr. Also, shorter right tails for the dissipation rates are observed for the data in the bulk in comparison with that for the whole cell. This was also observed by Emran & Schumacher (2008). This difference in the contribution to high-amplitude events between the bulk and the whole cell further motivates a more detailed statistical study at different heights for various Ra in a high-aspect-ratio cell.

The high-amplitude tails of the energy dissipation or local enstrophy PDFs, though associated with low-probability events, represent strong fluctuations. Therefore, they have received considerable attention, as they are important for understanding the intermittent and extreme behaviour in turbulent flows. These tails asymptotically follow stretched exponential forms (Donzis, Yeung & Sreenivasan 2008; Yeung *et al.* 2015; Xu, Zhang & Xia 2024). In contrast, the low-amplitude tails, despite being events with a higher probability, are much less studied. Recently, Gotoh & Yang (2022) and Gotoh, Watanabe & Saito (2023), using high resolution DNS of isotropic box turbulence, found that the left tail of kinetic energy dissipation and local enstrophy follow slopes of 3/2 and 1/2, respectively. To the best of our knowledge, this has not yet been reported in controlled laboratory experiments.

Estimating the dissipation or enstrophy using experimental methods such as single-point measurements of laser Doppler velocimetry (LDV) or hot-wire anemometry, combined with high temporal sampling rates and Taylor's hypothesis, is commonly used to estimate the kinetic energy dissipation. Also, two-point, three-point and multi-point LDV (Ducci & Yianneskis 2005) or hot-wire measurements have been used without relying on Taylor's

hypothesis, offering higher accuracy in estimating velocity gradients and dissipation in turbulent flows (Wallace & Vukoslavčević 2010). However, since the hot-wire method is intrusive, sensitive to orientation and its spatial resolution depends on the sensor area, it is not always the most suitable approach. Furthermore, non-invasive PIV, two-dimensional or stereoscopic, has been employed to estimate in-plane dissipation or pseudo-dissipation, which is particularly useful in homogeneous isotropic flows (Wang *et al.* 2021). In addition to computing velocity gradient components, planar PIV has the advantage of detecting flow structures but suffers from issues related to spatial resolution, particularly at high Rayleigh numbers (Kähler, Scharnowski & Cierpka 2012).

Recently, Xu *et al.* (2024) developed a novel PIV system, termed velocity-gradient-tensor-resolved PIV, designed to capture all nine components of the velocity gradient tensor at a single point. The system employs three lasers and three cameras, each aligned in three mutually orthogonal planes, and was applied to RBC in the range $2 \times 10^8 \leqslant Ra \leqslant 8 \times 10^9$. Using this set-up, they found the pseudo-dissipation near the bottom, centre and sidewall regions with an accuracy of approximately 3 %, significantly outperforming one-dimensional (1-D) and 2-D surrogate-based approaches. Furthermore, they reported scaling laws for the time-averaged kinetic energy dissipation rate with Ra that show good agreement with the predictions of the Grossmann–Lohse theory (Grossmann & Lohse 2000; Ahlers, Grossmann & Lohse 2009). Surprisingly, they found events near the sidewall to be highly intermittent compared with those in the bulk and near the bottom plate. The kinetic energy dissipation rate or / and enstrophy has also been extensively studied in various flows, including decaying grid turbulence (Liberzon *et al.* 2012), dilute polymer solutions (Liberzon *et al.* 2006) and Taylor–Couette flow (Tokgoz *et al.* 2012).

In this paper, we present intermittency statistics using all nine components of the velocity gradient tensor, as well as derived quantities such as the vorticity components, enstrophy and dissipation, in a $\Gamma = 25$ convection cell for $3.7 \times 10^5 \leqslant Ra \leqslant 4.8 \times 10^6$ and $5 \leqslant Pr \leqslant 7.1$. Results are presented at multiple heights in the bottom half of the convection cell. A spatio-temporally resolved 3-D velocity field was obtained using the Lagrangian particle tracking method, shake the box (*STB*) (Schanz, Gesemann & Schröder 2016). The Lagrangian particle data were further processed using the data reconstruction method Vortex-In-Cell (VIC#) to obtain the Eulerian velocity fields in multiple planes stacked over each other. These planes are parallel to the bottom plate. The spatial resolution of the resulting 3-D velocity field is of the order of the Kolmogorov length scale. The PDFs of all nine velocity derivatives are in good agreement with those from DNS at $Ra = 1 \times 10^6$ and $Pr = 6.6$. Using the experimental data, we discuss the small-scale intermittency statistics as a function of Ra, and compare the bulk statistics with those near the proximity of plate. To this end, we analyse the PDFs of all nine velocity gradients, three components of the vorticity vector, kinetic energy dissipation and local enstrophy. Intermittency increases with increasing Ra and in proximity to the heating plate. Additionally, we compare the left-tail scalings of the kinetic energy dissipation and enstrophy with the recent DNS results by Gotoh & Yang (2022). We also discuss other relevant statistical quantities.

The present paper is organised as follows. In § 2, we describe the experiments in detail. In § 3, we compare all nine velocity gradient components from one experiment with those from DNS at the same Ra and Pr. Further, using experimental results, we discuss the intermittency statistics of velocity gradients and vorticity components at the mid-height (§ 3.1) and in the z-direction in the bottom half of the cell (§ 3.2) for various Ra. Furthermore, in § 3.3, we discuss the PDFs of the kinetic energy dissipation and enstrophy and the left-tail scalings for them at various heights. Finally, we summarise the main results in § 4. In Appendix A, we briefly describe the DNS used for comparison.

The subsequent appendices provide additional statistical results that support the findings in the main text.

2. Experiments

To study the statistics of velocity derivatives, all nine components of the velocity gradient tensor were computed in the RBC cell. To this end, we obtain a 3-D velocity field using a time-resolved Lagrangian particle tracking velocimetry method employing *STB* and VIC#, both available in the software package Davis 10.2 (LaVision GmbH).

The RBC experiments were conducted in a convection cell with an aspect ratio of $\Gamma = 25$ and a height of $H = 28$ mm. A schematic of the experimental set-up is shown in figure 1(*a*). Water was used as the working fluid, confined between the cooling and heating plates. A constant temperature difference of $\Delta T = T_h - T_c$ was maintained between the heating and cooling plates, where T_h and T_c are the average temperatures of the heating and cooling plates, respectively. The sidewalls were vertical and adequately insulated to prevent heat loss. Additionally, the room temperature was maintained close to the bulk fluid temperature T_b, where $T_b = (T_h + T_c)/2$. The temperature of the cooling plate was measured using four PT-100 thermistors in contact with its surface, while the temperature of the heating plate was measured using five thermistors embedded within it. The average temperature at each plate was maintained constant and used for the calculation of ΔT. The physical properties of water were estimated at the bulk fluid temperature. The heating plate was made of aluminium, and its temperature was kept constant using a constant-temperature bath. The cooling plate was made of glass to allow optical access inside the convection cell. The temperature of the cooling plate was controlled by circulating cold water over it, supplied by a constant-temperature thermostat in a closed-loop system. The temperature difference ΔT was varied to change the Rayleigh number. The estimated values of Ra and Pr are listed in table 1. The maximum deviation in temperature measurements of individual sensors from the mean at the cold and hot plates was estimated. At $Ra = 3.7 \times 10^5$, 9.9×10^5 and 4.8×10^6, the deviations at the cold plate were 0.2, 0.3 and 0.5 K, respectively, while those at the hot plate were 0.06, 0.07 and 0.5 K, respectively. Except for the highest Ra experiment, the temperature of the hot plate was uniformly maintained within the measurement accuracy. At the highest Ra, the maximum deviation in recorded temperatures at the hot plate for any sensor from its mean was within ± 0.05 K, indicating a relatively uniform local temperature. This suggests that, while temperature remains approximately constant in the local regions, there is a slight gradient from the centre toward the sides. Since our measurements are focused near the central region (130 mm $\times$ 125 mm), which covers less than 4 % of the total area, we can reasonably assume the temperature in the measurement zone to be approximately uniform. Even though isothermal conditions at the plates are not exactly maintained, the deviations from the mean remained small relative to ΔT. The effects of non-ideal boundary conditions at the plates on the flow dynamics and heat transfer are discussed in Käufer *et al.* (2023) and Vieweg *et al.* (2025). Additional details of the convection cell can be found in Moller *et al.* (2020, 2021).

The flow was seeded with neutrally buoyant polyamide particles of diameter 55 μm and density $\rho_p = 1.01$ g cm^{-3}. The estimated Stokes number at the highest $Ra = 4.8 \times 10^6$ was 2×10^{-4}; hence, the particles followed the flow faithfully. The particles were first mixed thoroughly with water using a magnetic stirrer, and the mixture was allowed to stabilise in a beaker. After approximately half an hour, some particles floated on the water surface, some settled at the bottom, while the neutrally buoyant ones remained suspended.

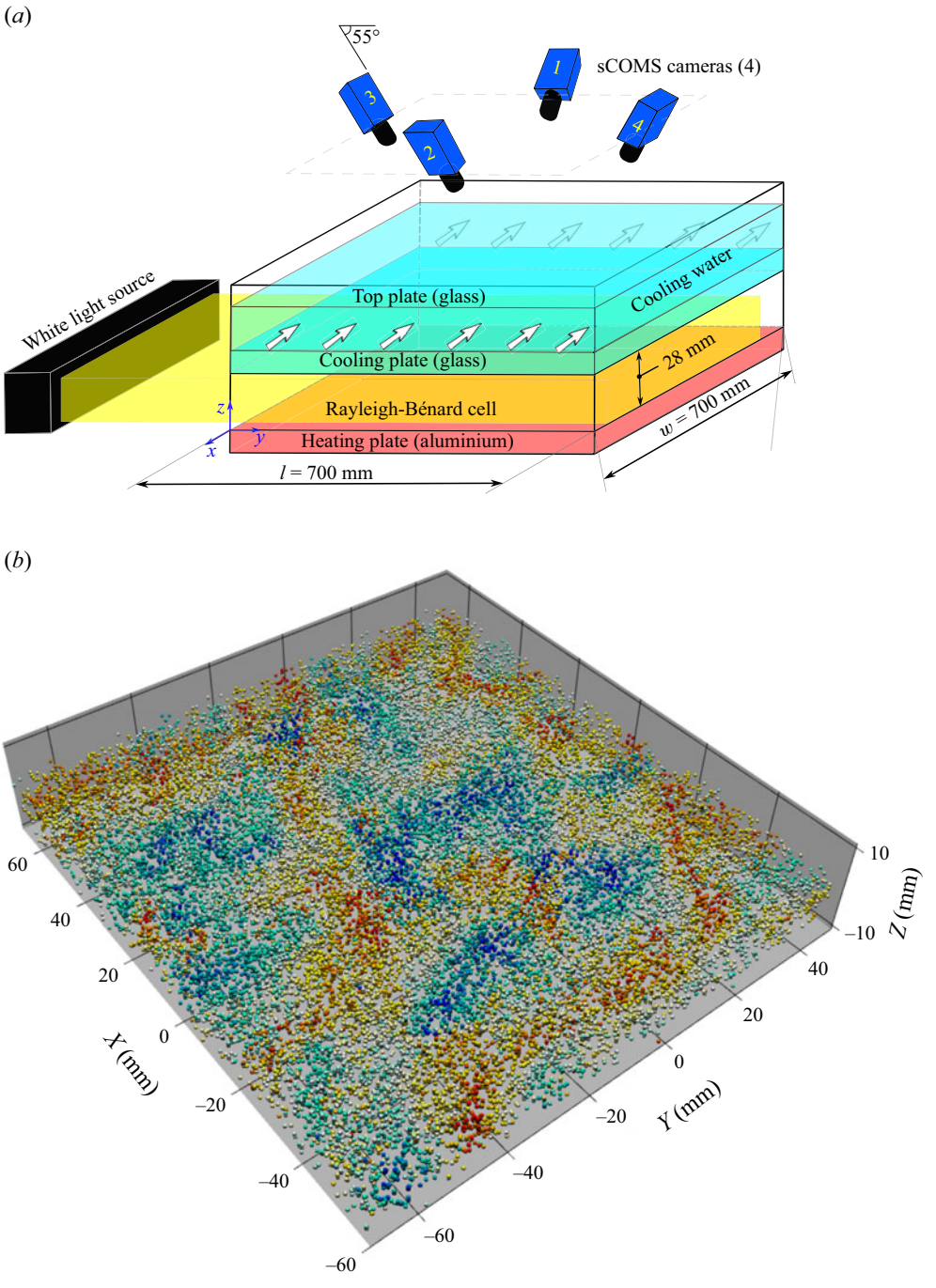

Figure 1. (*a*) Schematic of the experimental set-up of the RBC and (*b*) snapshot showing particles in the measurement volume in the bottom half of the cell at $Ra = 4.8 \times 10^6$. Particles are coloured according to their vertical velocities, with red and yellow indicating positive values, while cyan and blue indicate negative ones. Velocity varies between -6.5 and 6 mm s^{-1}. The bottom plate is located at $Z = -11$ mm. Clearly visible is the turbulent superstructure pattern of the up- and downflows.

Expt. No.	Ra	Pr	T_h °C	T_c °C	ΔT °C	fps Hz	t_f S	T_f	Tracked Particles	η_k Mm	Δx^{Eul} Mm	PPUC Particles	N_{snap}
Set 1													
1	3.7×10^5	7.1	20.21	18.85	1.36	11	3.37	540	22 k	1.9	1.1	0.18	4000
2	5.3×10^5	7.2	20.00	17.95	2.05	15	2.82	213	30 k	1.7	1.1	0.25	2250
3	1.0×10^6	6.6	23.57	20.48	3.08	16	2.11	267	29 k	1.4	1.1	0.24	3000
Set 2													
4	3.7×10^5	7.1	20.18	18.86	1.33	11	3.40	240	27 k	—	1.4	0.20	2250
5	9.9×10^5	6.6	23.53	20.49	3.04	16	2.12	265	16 k	—	1.7	0.21	2250
6	4.8×10^6	5.0	37.20	29.41	7.79	20	1.08	325	33 k	0.8	1.1	0.13	1750

Table 1. Values of the experimental parameters measured. Lagrangian particle tracking measurements were conducted in two sets: set 1 measurements were taken within a ±5 mm thick illuminated volume around the central z-plane, while set 2 measurements were taken in a 20 mm thick illuminated volume extending from the heating plate into the bulk. In all experiments the field of view (FOV) was $130 \times 125\,\mathrm{mm}^2$; the FOV is common to all four cameras. Here, PPUC refers to the average number of tracked particles within a unit cell, used to determine a velocity vector and N_{snap} denotes the number of snapshots of the Eulerian field used in each z-plane.

Particle suspension from the central section was then extracted and used for seeding. This method ensured that the floating and settling particles were filtered out, retaining only the neutrally buoyant ones (Shevkar *et al.* 2019). The seeding particles added into the flow were illuminated within a volume using a pulsed white light LED source, see Moller, Resagk & Cierpka (2020). The particle scattering images were captured as a time series using four sCMOS cameras (2560 × 2160 pixels) from the top of the cell through an imaging window of size 25 cm × 25 cm. The cameras were positioned at an angle of approximately 35° to the vertical axis in a symmetric arrangement. All cameras were equipped with 100 mm focal length optics (Zeiss Milvus 2 / 100 M). Additionally, these lenses were mounted on the cameras via Scheimpflug adapters to optimise the depth of the field.

The calibration was carried out in the middle of the cell using a 3-D calibration plate (No. 204-15, by LaVision) under actual experimental conditions using a polynomial function. During calibration, the top plane of the plate was positioned at the mid-z plane. The images were masked to a common area imaged by all four cameras. Additionally, the images were pre-processed before performing volume self-calibration (Wieneke 2008) and the calibration of particle imaging steps (Schanz *et al.* 2012).

Using time-resolved camera images ($1/t_f \ll$ fps) and the generated calibration function, the positions of the particles were computed using *STB*, where t_f is the free-fall time in seconds and fps stands for frames per second of imaging. An instantaneous 3-D particle field coloured by vertical velocities in the bottom half of the cell is shown in figure 1(*b*). The yellow–red particles, indicating positive vertical velocities, form a connected structure, while the cyan–blue particles, representing negative vertical velocities, form another one. Together, most likely they contribute to a larger, organised superstructure in turbulent convection (Pandey *et al.* 2018; Stevens *et al.* 2018; Vieweg, Scheel & Schumacher 2021; Moller *et al.* 2022; Weiss *et al.* 2023; Ettel, Vieweg & Schumacher 2025). The particles were tracked for up to 100 time steps. The total numbers of tracked particles in the current experimental study for various experiments are listed in table 1. These are the average number of Lagrangian trajectories per snapshot. By fitting a third-order polynomial through the obtained particle positions on a distinct trajectory, the velocities and accelerations of the particles at different locations in the flow field were estimated. A variable time-step processing approach was employed, with an

allowed triangulation error of around one voxel. Velocity limits in the x- and y-directions (horizontal coordinate axes) were set based on the maximum particle displacement per unit time in the horizontal plane, while the limit in the z-direction (vertical coordinate axis) was determined using a trial-and-error method. Here, $x = X/H$, $y = Y/H$ and $z = Z/H$ where X, Y and Z are dimensional coordinates. The acceleration limit was set based on the maximum of the above velocity limits. With manual inspection of the flow field, a decision was made on the use of a spatial filter to remove spurious tracks. Particles not in agreement with the neighbourhood were removed in this step. Removing these outliers was important to achieve statistical convergence of the velocity gradients, even though they occurred only at a few locations at any given instant within the volume. The allowed triangulation error and the required number of iterations of a spatial median filter during post-processing were optimised to detect true particles while effectively removing spurious tracks. At the highest $Ra = 4.8 \times 10^6$, the average uncertainty in the Lagrangian particle velocity magnitude was 13.3 %. This value was calculated from all particles within the measurement volume from a randomly selected 100 consecutive time instants. The distribution of percentage uncertainty was right skewed with a peak at 5.6 %, indicating that most uncertainty values were relatively small. A small fraction of particles displayed high uncertainty values originated from particles with near-zero displacement for any given time step. Additionally, the median percentage uncertainty was 8.9 %. This median error in our analysis using a third-order polynomial is of the same order as those reported in the literature for a second-order polynomial (Rockstroh & Michaelis 2021). Similar trends were observed for other two Ra cases.

Furthermore, Eulerian velocity data were obtained by processing particle tracks from *STB* in the VIC# software (Jeon, Müller & Michaelis 2022; Wang, Liu & Wang 2022) by solving the cost function for at least 120 iterations. Here, VIC# interpolates the Lagrangian data to the grid and employs optimisation algorithms to enforce compliance with the governing equations of the fluid motion. This inherently introduces a negative bias error in the vorticity magnitude, reported to be of the order of approximately 2 %, with the largest effects occurring near solid boundaries (Sciacchitano, Leclaire & Schröder 2021). To minimise this influence, we excluded the two planes closest to the plate from our analysis. Any bias error in vorticity magnitude, if present, does not qualitatively alter the trends observed in our results. The processing resulted in grid data in the horizontal plane, with several planes stacked on top of each other. Each horizontal plane in set 1 experiments resulted in a resolution of 1.1 mm with 121 × 116 vectors. The 3-D vector resolution, Δx^{Eul}, on a 3-D Eulerian grid for both sets of experiments at various Ra is listed in table 1. The data quality was the same in all three directions. We also list the Kolmogorov length η_k for various Ra using

$$\eta_k = \left(\frac{Pr}{Ra}\right)^{3/8} \langle \epsilon \rangle_{A,t}^{-1/4}, \tag{2.1}$$

where $\langle \epsilon \rangle_{A,t}$ is the combined area-time average of the dimensionless kinetic energy dissipation rate at the mid-height (Scheel *et al.* 2013). Characteristic units are ΔT for temperature, $U_f = \sqrt{g\alpha \Delta T H}$ for velocity and H for length, where U_f is the characteristic free-fall velocity. The values of the resulting free-fall time, $t_f = H/U_f$, and total recording time in free-fall units, T_f, for different experiments are also listed in table 1. Based on the number of vectors and total number of tracked particles in a volume for each experiment, particles per unit cell (PPUC) are estimated. In our experiments, PPUC values are ranged in between 0.13 and 0.25. This corresponds to approximately 4–8 velocity vectors per particle, which is consistent with previously reported practices (Schanz *et al.* 2016; Jeon *et al.* 2022).

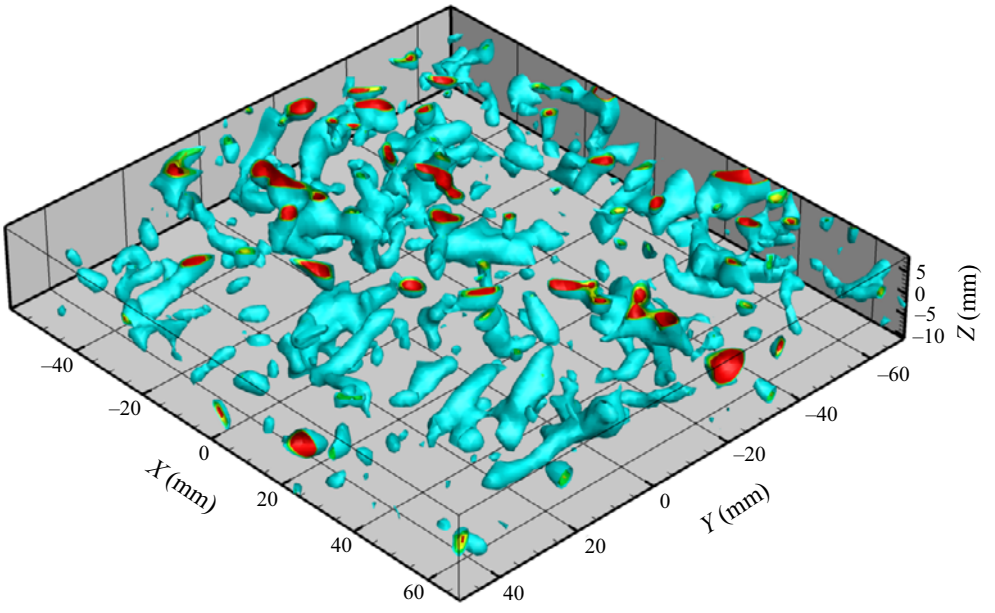

Figure 2. Vortical structures by Q-criterion at a randomly chosen time instance for $Ra = 4.8 \times 10^6$ and $Pr = 5$ within the measurement volume. The iso-surfaces of Q within the range of 0.3 and 0.5 (cyan–green–yellow–red) are shown.

During each experimental run, temperature control devices, which are connected to the heating and cooling circuits, were set to the desired values. Once a steady state was reached, test fluid with particles was injected into the flow through a tube connected to the convection cell, and the excess water (approximately 500 ml) was drained using a tube connected to the other side of the cell. The flow was then allowed to stabilise for half an hour, followed by recordings at the optimal frame rate (fps) for the particle tracking experiments. Figure 2 shows the isosurfaces of vortical structures at a time instant taken in the RBC experiment. We display isosurfaces in correspondence with the Q-criterion (Chong, Perry & Cantwell 1990), which are obtained by

$$Q = \frac{1}{2}(O_{ij}O_{ji} - S_{ij}S_{ji}) \quad \text{with} \quad O_{ij} = \frac{1}{2}\left(\frac{\partial u_i}{\partial x_j} - \frac{\partial u_j}{\partial x_i}\right). \tag{2.2}$$

The tangle of characteristic elongated tube-like structures becomes visible in the bulk, even though Reynolds numbers are relatively low for the present high-Prandtl-number case.

3. Results

In our convection experiments, Eulerian velocity fields were obtained for at least 200 free-fall times at all Ra, ensuring that the data records are long enough to provide reliable statistics. First, we present the statistical results at the mid-height of the convection cell. Here mid-height refers to the planar cross-section at the mid-height.

3.1. *Velocity derivative statistics in the midplane*

The obtained velocity fields are well resolved while also being comparable to the Kolmogorov length scale η_k. The values of grid resolution and the length scale η_k were

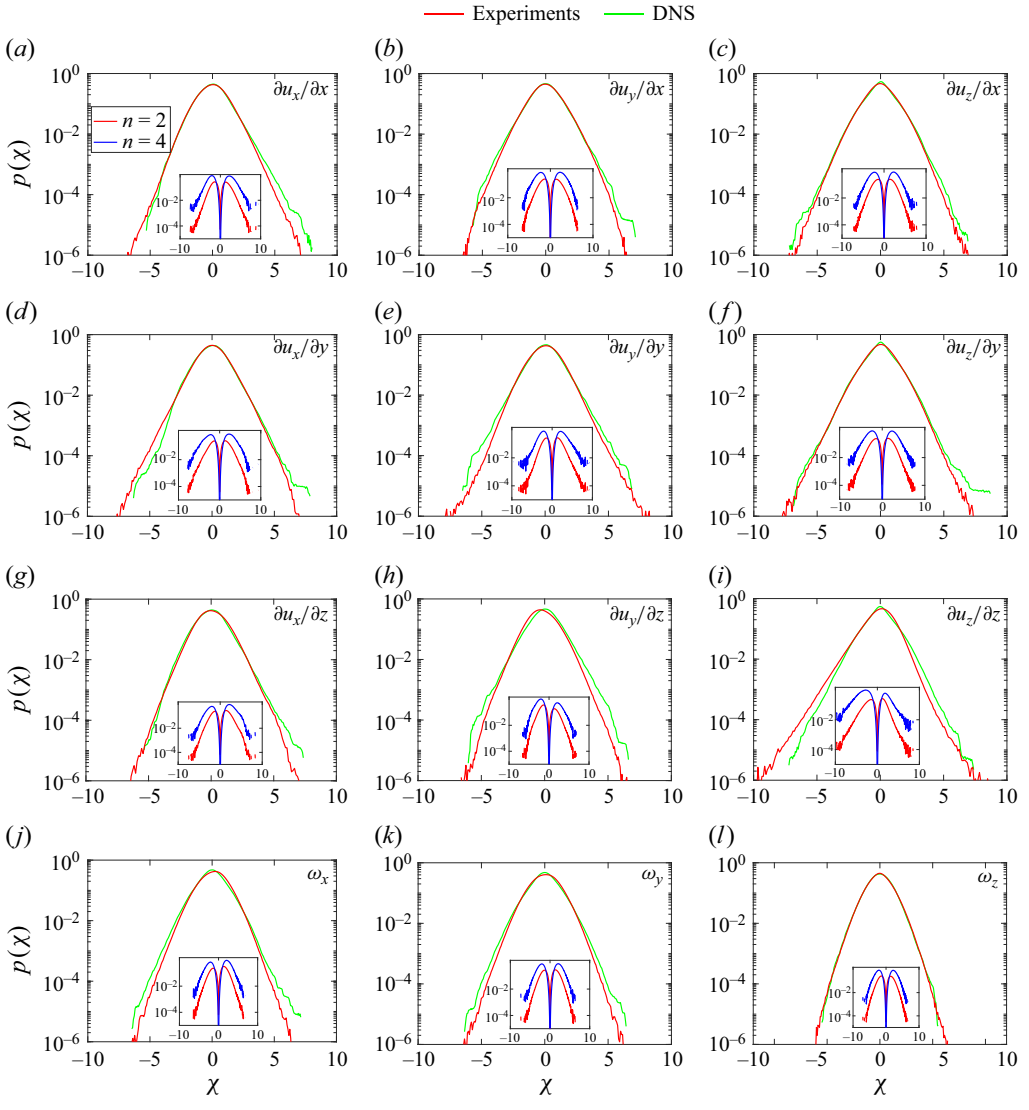

Figure 3. Comparison of PDFs $p(\chi)$ of the nine velocity gradient tensor components and three vorticity components between experiment and direct numerical simulation, see also Appendix A. Data are obtained at the mid-plane for $Ra = 1.0 \times 10^6$ and $Pr = 6.6$. The quantities shown are $\partial u_x/\partial x$ in (*a*), $\partial u_y/\partial x$ in (*b*), $\partial u_z/\partial x$ in (*c*), $\partial u_x/\partial y$ in (*d*), $\partial u_y/\partial y$ in (*e*), $\partial u_z/\partial y$ in (*f*), $\partial u_x/\partial z$ in (*g*), $\partial u_y/\partial z$ in (*h*), $\partial u_z/\partial z$ in (*i*), ω_x in (*j*), ω_y in (*k*) and ω_z in (*l*). All quantities are normalised by their respective root-mean-square (r.m.s.) values. Inset figures show the statistical convergences of higher-order velocity derivative statistics for the experimental results shown in the main figures. We plot $\chi^n p(\chi)$ versus χ. Here, $n = 2$ and 4 for red and blue solid lines, respectively. Note that the y-axis is in logarithmic units.

calculated using (2.1) for various Ra at mid-height, and are listed in table 1. We define

$$\chi = \frac{\omega_i}{\sqrt{\langle \omega_i^2 \rangle_{A,t}}} \text{ or } \chi = \frac{\partial u_i/\partial x_j}{\sqrt{\left\langle \left(\partial u_i/\partial x_j\right)^2 \right\rangle_{A,t}}}, \tag{3.1}$$

with $i, j = 1, 2, 3$. Note that quantities in (3.1) are normalised by their respective root-mean-square (r.m.s.) values. Figure 3 compares the experimentally obtained PDFs with

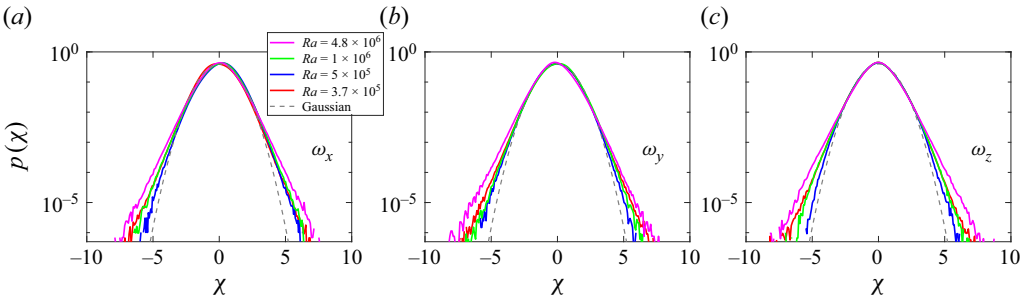

Figure 4. Probability density functions of vorticity components at the mid-plane for four different Ra. The quantities shown are ω_x in (a), ω_y in (b) and ω_z in (c).

those from DNS, obtained in the mid-height for $Ra = 1 \times 10^6$ and $Pr = 6.6$. The nine velocity derivatives and three vorticity components are plotted. The experimental data show good agreement with the DNS results, except in some of the far tails. A detailed description of the DNS is presented in Appendix A. The good agreement between the experimental data and DNS results reflects the rigour of the experimental measurements and the robustness of the data processing methodology. The insets of figure 3 demonstrate statistical convergence for the gradient components presented in the respective main figures from the experiments. The decay of higher-order moments towards zero in the log–lin plot of $\chi^n p(\chi)$ vs. χ, for both $n = 2$ and $n = 4$, indicates sufficient statistical sampling and proper resolution of small-scale structures in the flow. The higher-order moments of $\partial u_z/\partial z$ further unveil highly left skewed nature of $\partial u_z/\partial z$ at the mid-plane, as seen in the inset of figure 3(i). This left skewed profile is likely due to the cold and hot plumes plunging into the bulk. Interestingly, gradients of velocities in z-direction seem to be more skewed compared with those in the x- and y-directions, which we also discuss using quantitative analysis later in § 3.2. Similar to $Ra = 1 \times 10^6$, the statistical convergence at the highest $Ra = 4.8 \times 10^6$ is illustrated in Appendix B.

Figure 4 shows the PDFs of vorticity components in x-, y- and z-directions at the mid-height for four different Ra values, spanning an order of magnitude from the lowest $Ra = 3.7 \times 10^5$ to the highest $Ra = 4.8 \times 10^6$ using the experimental data. The Gaussian distributions are also included in the figures as dashed lines for comparison with the PDFs. All the PDFs of vorticity components ω_x, ω_y and ω_z exhibit non-Gaussian behaviour with tails which become increasingly wide as Ra number increases. These wider tails in the PDFs of ω_i are the signatures of increasing small-scale intermittency, similar to the non-Gaussian intermittent velocity derivative statistics discussed in Schumacher *et al.* (2014, 2018). Interestingly, the shapes and extents of PDFs of different components of vorticity at same Ra are similar. This suggests that the dominant vorticity structures at mid-height are likely small and do not favour any particular direction for the range of Ra, Pr and $\Gamma = 25$ convection cells in the current investigation.

3.2. *Velocity derivative statistics with respect to the z-direction*

To study derivative statistics in the z-direction at each Ra, we discuss the PDFs of the velocity derivatives and resulting higher-order statistical quantities at four different planes. Details of these planes for three different Ra are given in table 2. These planes are chosen from the bottom half of the convection cell due to the complete availability of data in this region and the symmetry of the flow about mid-height in RBC. One of these plane locations is chosen close to the mid-height. The other three planes are chosen such that their height, when normalised by the thermal boundary layer thickness, remains the same

$Ra = 3.7 \times 10^5$					$Ra = 9.9 \times 10^5$					$Ra = 4.8 \times 10^6$				
z	z/δ_T	G_{11}	G_{22}	$\frac{G_{11}+G_{22}}{2}$	z	z/δ_T	G_{11}	G_{22}	$\frac{G_{11}+G_{22}}{2}$	z	z/δ_T	G_{11}	G_{22}	$\frac{G_{11}+G_{22}}{2}$
0.51	7.1	2.00	1.29	1.65	0.50	8.9	1.89	0.94	1.42	0.48	13.0	0.87	0.75	0.81
0.42	5.7	2.02	1.35	1.69	0.33	5.8	1.58	0.96	1.27	0.21	5.7	0.94	0.90	0.92
0.27	3.7	1.48	1.33	1.41	0.21	3.7	1.28	1.09	1.19	0.14	3.6	1.00	0.96	0.98
0.17	2.4	0.74	0.94	0.84	0.15	2.6	0.88	0.74	0.81	0.10	2.6	0.90	0.82	0.86
0.12	1.7	0.67	0.69	0.68	—	—	—	—	—	—	—	—	—	—

Table 2. List of x-y plane locations selected for the analysis and corresponding anisotropy coefficients at three different Ra. Here, δ_T was estimated using an expression of dimensionless heat flux $Nu = 0.33 Ra^{1/4} Pr^{-1/12}$, see Grossmann & Lohse (2000).

for each Ra. The values of the normalised heights z/δ_T of those planes are approximately 2.6, 3.7 and 5.6, and are also specified in table 2. This corresponds to $z = 0.1$, 0.14 and 0.21 at the highest Ra. The thermal boundary layer thickness was estimated using the Nusselt number correlation (specified in caption of table 2) given by Grossmann & Lohse (2000).

3.2.1. *Local isotropy in convection flow*

We quantify the degree of anisotropy in second-order derivatives using the ratios

$$G_{ij} = \frac{\left\langle (\partial u_i/\partial z)^2 \right\rangle (1+\delta_{iz})}{\left\langle (\partial u_i/\partial x_j)^2 \right\rangle (1+\delta_{ij})} \quad \text{with} \quad i,\, j = x,\, y,\, z, \tag{3.2}$$

as given in Vorobev *et al.* (2005). Note also that, for the indices i, j, k, the spatial directions x, y, z correspond to 1, 2, 3, respectively. Both notations are used. Here, δ_{ij} denotes the Kronecker delta, which equals 1 when $i = j$ and 0 otherwise. Flows with $G_{ij} = 1$ are perfectly isotropic flows while the $G_{ij} \to 0$ are strongly anisotropic. The calculated values of G_{11}, G_{22} and the mean of both in our experiments are listed in table 2 . Here, G_{11} and G_{22} relate the transverse derivatives of the in-plane velocity components with respect to z, compared with their corresponding in-plane derivatives. They are given by

$$G_{11} = \frac{\left\langle (\partial u_x/\partial z)^2 \right\rangle}{2\left\langle (\partial u_x/\partial x)^2 \right\rangle} \quad \text{and} \quad G_{22} = \frac{\left\langle (\partial u_y/\partial z)^2 \right\rangle}{2\left\langle (\partial u_y/\partial y)^2 \right\rangle}. \tag{3.3}$$

These anisotropic coefficients take values close to one at all heights for the three Ra, indicating slight deviation from isotropy. The deviation in the values among the three considered Ra is highest at the lowest $Ra = 3.7 \times 10^5$, and the flow becomes increasingly isotropic with increasing Ra in the bulk.

3.2.2. *Velocity gradients*

Figure 5 shows the PDFs of four representative velocity gradient tensor components, two in the x-direction and the other two in the z-direction, at the highest $Ra = 4.8 \times 10^6$. Firstly, the PDFs at all heights in the bottom half of the convection cell show non-Gaussian intermittent velocity derivative statistics. The PDFs of $\partial u_x/\partial x$ and $\partial u_y/\partial x$ show tails that become somewhat wider as we move closer to the plate, for both the left and right tails of the distribution. This is again a clear sign of increased intermittency near the plate compared with the mid-height.

In contrast, the right and left tails in the PDFs of $\partial u_x/\partial z$ and $\partial u_z/\partial z$ do not show any systematic behaviour as we move closer to the bottom plate. The right tail becomes increasingly wide as we approach the plate, while the left one shows the opposite

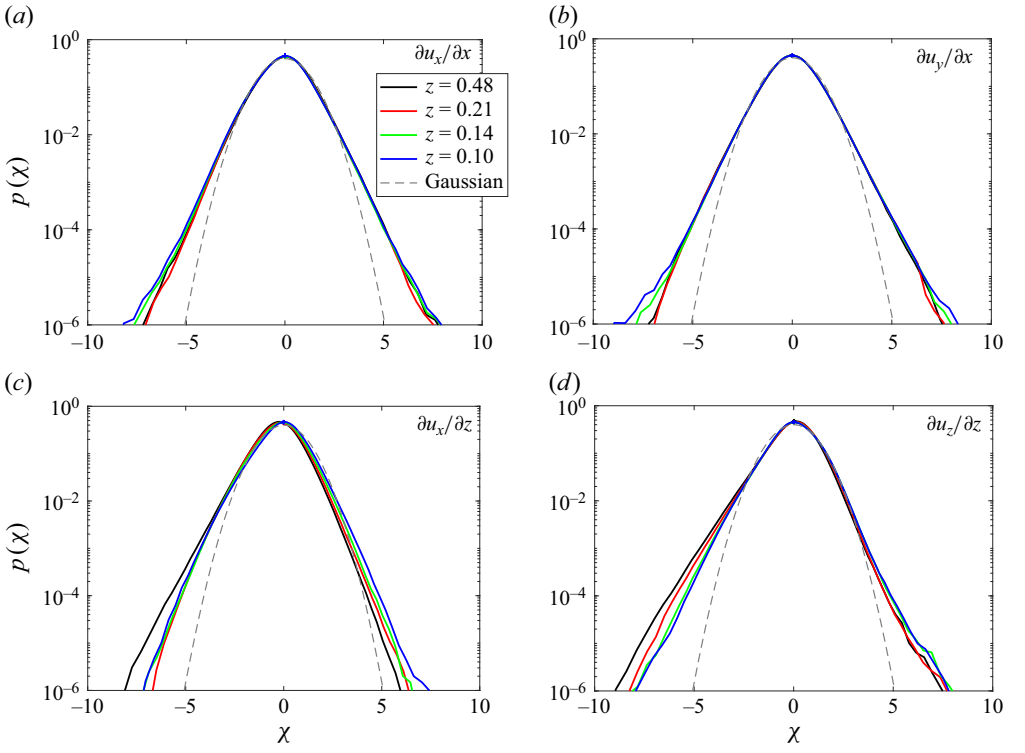

Figure 5. Probability density functions of velocity gradients for four different planes in the z-direction at the highest $Ra = 4.8 \times 10^6$. The quantities shown are $\partial u_x/\partial x$ in (*a*), $\partial u_y/\partial x$ in (*b*), $\partial u_x/\partial z$ in (*c*) and $\partial u_z/\partial z$ in (*d*). Lines show, $z = 0.48$ (black line), $z = 0.21$ (red line), $z = 0.14$ (green line), $z = 0.10$ (blue line) and Gaussian reference (dashed, grey line). The binning for the PDF calculation is logarithmic with smaller bins near the centre.

behaviour. Partially, this is because the PDFs of $\partial u_z/\partial z$ become less left skewed as we move toward the plate. The other gradients in the horizontal and vertical directions show similar tail behaviour, as described above in figures 5(*a*,*b*) and 5(*c*,*d*), respectively. Similarly, the tail behaviour in the other two lower Ra listed in table 2 follows a similar trend for different planes in the bottom half of the convection cell, as observed at the highest Ra.

In our analysis, the PDF tails of velocity gradients in the bulk follow an exponential distribution, consistent with Xu *et al.* (2024), whereas this behaviour is generally not observed near the plates.

We calculate the skewness of velocity gradients $S_3 = \langle \chi^3 \rangle / \sigma^3$ to quantify the asymmetry of their distributions. Figure 6 shows the skewness values of the gradient components in the bottom half of the convection cell at three Rayleigh number values, namely $Ra = 3.7 \times 10^5$, 9×10^5 and 4.8×10^6. The velocity derivatives are grouped into five natural pairs with the same statistics. This grouping is done for symmetry reasons and improves statistical convergence.

Skewness of horizontal derivatives—The PDFs of transverse derivatives in the x- and y-directions at different z-locations exhibit an approximately symmetric nature, which is shown in figure 6(*a*,*b*,*d*). The skewness values confirm this, as they mostly remain close to zero, ranging between -0.1 and 0.1. The skewness values of the pair of derivatives, $\partial u_z/\partial x$ and $\partial u_z/\partial y$, are independent of Ra. In comparison, the skewness values of the

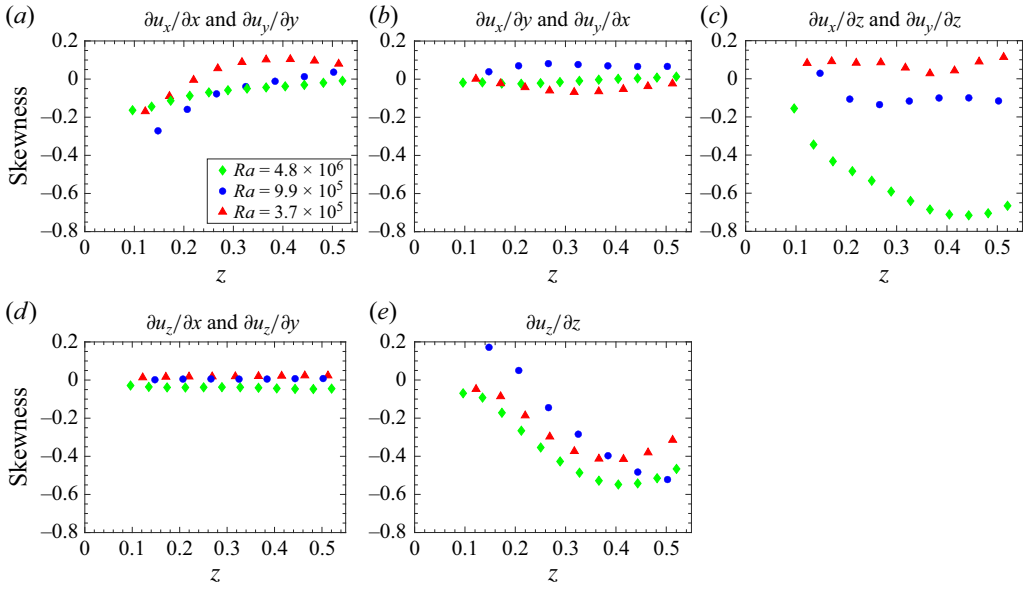

Figure 6. Skewness of velocity derivatives, $S_3 = \langle \chi^3 \rangle / \sigma^3$ at multiple planes in the z-direction for three different Ra. Here, σ is the standard deviation of χ. The quantities shown are $\partial u_x/\partial x$ and $\partial u_y/\partial y$ in (a), $\partial u_x/\partial y$ and $\partial u_y/\partial x$ in (b), $\partial u_x/\partial z$ and $\partial u_y/\partial z$ in (c), $\partial u_z/\partial x$ and $\partial u_z/\partial y$ in (d) and $\partial u_z/\partial z$ in (e). Red triangles, $Ra = 3.7 \times 10^5$; blue circles, $Ra = 9.9 \times 10^5$; green diamonds, $Ra = 4.8 \times 10^6$.

longitudinal derivative pair $\partial u_x/\partial x$ and $\partial u_y/\partial y$ at different Ra take increasingly negative values closer to the heating plate, with the highest value approaching -0.3, as seen in figure 6(a). These negatively skewed values for the normal strain components near the heating plate are associated with the events of vigorous plume detachments from the boundary layers close to the heating plate. Plumes are known to contribute to the largest thermal dissipation events near the plate (Emran & Schumacher 2012). Furthermore, in the horizontal analysis plane closest to the plate, plumes are the regions of negative horizontal divergence (Shevkar *et al.* 2022). This implies that the flow strongly decelerates in the horizontal direction, likely causing negatively skewed PDFs of normal strains.

Skewness of vertical derivatives—The PDFs of derivatives with respect to the z-direction are close to symmetric near the heating plate; they become increasingly negatively skewed (and thus asymmetric) deeper into the bulk. Most likely, the descending cold plumes, after detaching from the top wall into the bulk, are responsible for the far left-tail events in those components of the gradient tensor. Hot and cold plumes organise themselves to form LSCs. Thus, this result indicates a reduced influence of the LSC on the local flow dynamics as we move away from the mid-height towards the plates. The derivative skewnesses in panels (c,e) also show a strong dependence on Ra. The pair $\partial u_x/\partial z$ and $\partial u_y/\partial z$ takes skewness values of $S_3 = -0.15$ near the plate, which decrease to -0.7 at the mid-height for the largest Rayleigh number. Following a similar trend, $\partial u_z/\partial z$ at all three Ra values shows a skewness value approaching -0.5 at mid-height, which is a typical magnitude of the longitudinal derivative skewness of HIT. Mean values of skewness for the vertical longitudinal derivative $\partial u_z/\partial z$ in the bulk of the cell increase in magnitude from $S_3 = -0.37$ at the lowest $Ra = 3.7 \times 10^5$ to $S_3 = -0.49$ at the highest $Ra = 4.8 \times 10^6$, see table 3. These mean values are calculated over the height range of $0.25 \leqslant z \leqslant 0.5$.

Similarly, we calculate the flatness values of the velocity gradients by grouping them into five pairs. Figure 7 shows the flatness values at different z-planes in the bottom half

Ra	3.7×10^5	9.9×10^5	4.8×10^6
Skewness S_3	-0.37 ± 0.05	-0.37 ± 0.16	-0.49 ± 0.06
Flatness F_4	3.85 ± 0.05	4.03 ± 0.15	4.66 ± 0.13

Table 3. The mean values of skewness and flatness for $\partial u_z/\partial z$ in the bulk of the cell, calculated over the height range $0.25 \leqslant z \leqslant 0.5$ along with the corresponding maximum errors.

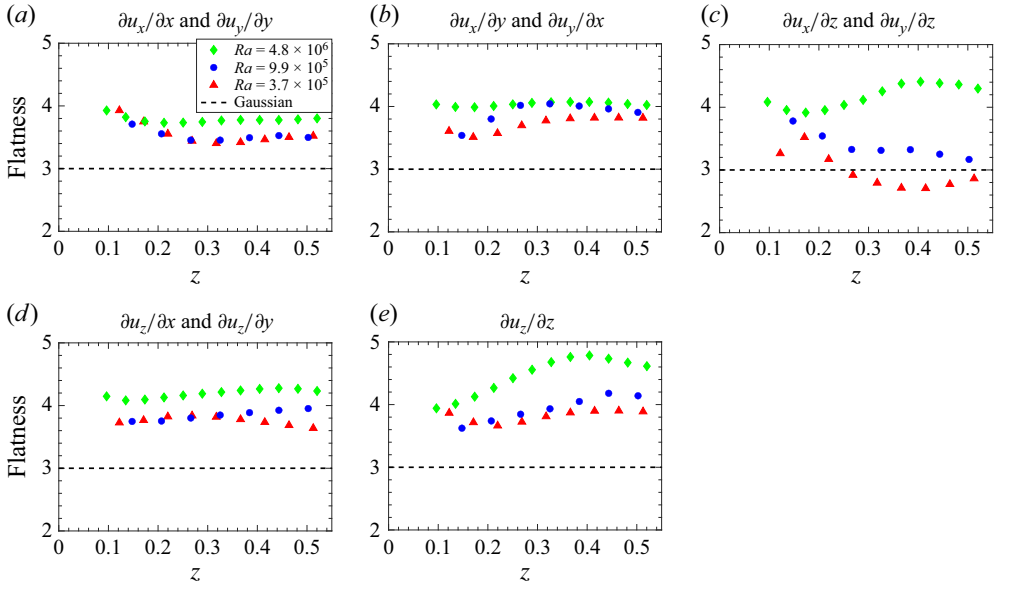

Figure 7. Flatness of velocity derivatives, $F_4 = \langle \chi^4 \rangle / \sigma^4$ at multiple planes in the z-direction for three different Ra. The quantities shown are $\partial u_x/\partial x$ and $\partial u_y/\partial y$ in (*a*), $\partial u_x/\partial y$ and $\partial u_y/\partial x$ in (*b*), $\partial u_x/\partial z$ and $\partial u_y/\partial z$ in (*c*), $\partial u_z/\partial x$ and $\partial u_z/\partial y$ in (*d*) and $\partial u_z/\partial z$ in (*e*). Red triangles, $Ra = 3.7 \times 10^5$; blue circles, $Ra = 9.9 \times 10^5$; green diamonds, $Ra = 4.8 \times 10^6$, Gaussian value of flatness is three (dashed line).

of the convection cell for three different Ra. For a Gaussian field, the flatness takes a value of $F_4 = 3$. Flatness values greater than three in the bottom half of the convection cell indicate non-Gaussian and intermittent velocity derivative statistics for the range of Ra and Pr considered in the present study. Increased flatness values with increasing Ra are due to the growing small-scale fluctuations which are associated with higher Ra, which were also evident in the tails of the vorticity PDFs, as shown previously in figure 4.

Flatness of horizontal derivatives—The variation of the flatness F_4 with increasing Ra is small and varies slightly with height for the derivative pairs in figure 7(*b*,*d*). However, the statistics for the pair of longitudinal derivatives, $\partial u_x/\partial x$ and $\partial u_y/\partial y$, show a weak, but systematic increase towards the plate for all three Ra, indicating slightly enhanced small-scale intermittency in that region, see panel (*a*). This is again likely due to plume detachment events.

Flatness of vertical derivatives—The increase in flatness values of vertical derivatives with increasing Ra seems to be more significant; in particular, the profiles for the largest Rayleigh number can be distinguished from the other data records. A variation at the value $F_4 \approx 4$ is observable for $\partial u_x/\partial z$ and $\partial u_y/\partial z$ for $Ra = 4.8 \times 10^6$ in panel (*c*). The flatness of $\partial u_z/\partial z$ for this Rayleigh number grows more strongly from the plate into the bulk, as

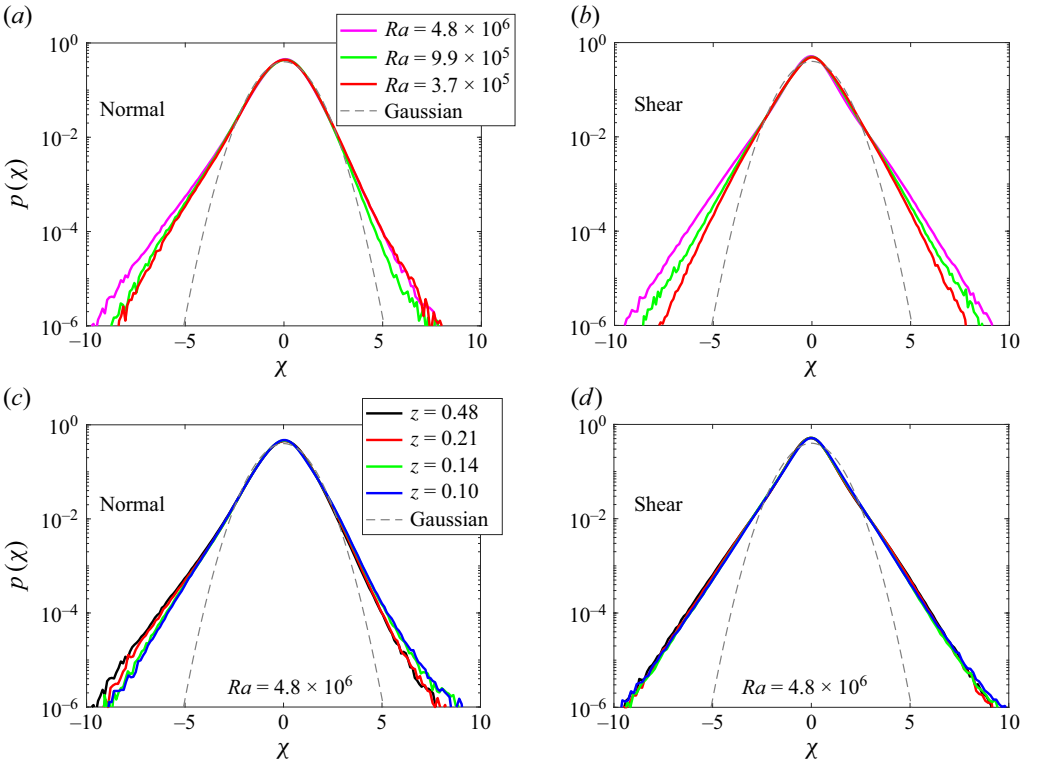

Figure 8. The PDFs of velocity gradients at the mid-plane for three different Ra. The velocity derivatives are grouped into normal (a) and shear (b) components. The PDFs are obtained from the three normal components ($i = j$) and the six shear components ($i \neq j$). Panels (c) and (d) show the PDFs of velocity gradients at four different heights in the z-direction for the highest $Ra = 4.8 \times 10^6$, again grouped into normal and shear components, respectively. The heights are $z = 0.48$ (black), $z = 0.21$ (red), $z = 0.14$ (green) and $z = 0.10$ (blue). In all panels, the Gaussian reference is shown as a dashed grey line.

seen in panel (e), reaching almost $F_4 \approx 5$. For the bulk averages, we find a growth from $F_4 = 3.85$ at the lowest $Ra = 3.7 \times 10^5$ to 4.66 at the highest $Ra = 4.8 \times 10^6$, see table 3. For all the normalised derivative moments, which we discussed in the last paragraphs, we have to keep in mind that the Rayleigh numbers are moderate; thus the resulting Reynolds numbers for the present $Pr > 1$ case lead rather to a three-dimensional time-dependent rather than a fully developed turbulent flow in the bulk of the convection layer.

3.2.3. *Comparison with recent experimental results*

Following Xu *et al.* (2024), we now plot the PDFs of velocity gradients grouped into normal (three components) and shear (six components) pairs, using data in the bottom half of the convection cell from set 2 (see table 1). Their measurements were carried out for $1.9 \times 10^8 \leqslant Ra \leqslant 9.4 \times 10^9$ and at three locations: one in the bulk, one close to the sidewall and a third point 5 mm above the bottom plate, outside the viscous boundary layer. The corresponding location of the bottom point at the lowest Ra of their measurements was at $z/\delta_T \approx 5$ (Shang, Tong & Xia 2008). Since major changes in the PDF tails are observed for $z/\delta_T \leqslant 3.7$ and relatively lower Ra in our study, we compare our results mainly for measurements in the bulk.

Figure 8(a–b) shows the mid-plane PDFs for three different Ra. The normal components are left skewed, whereas the shear components are symmetric, consistent

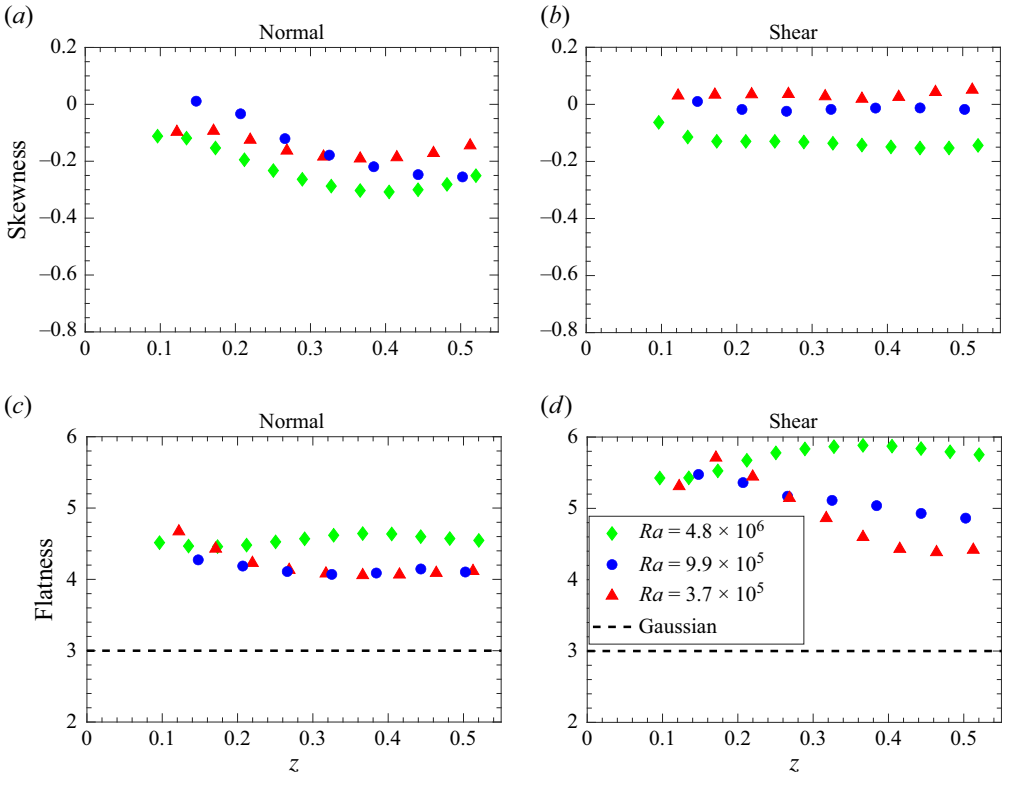

Figure 9. Skewness and flatness values for the velocity derivatives for three different Ra. Velocity derivatives are grouped into two as normal (a,c) and shear (b,d) components, consisting of diagonal and off-diagonal terms of the velocity gradient tensor, respectively. The mean skewness of either the three normal components or the six shear components is considered here.

with Xu *et al.* (2024). Additionally, the PDF tails of both the normal and shear components follow the exponential distribution. Unlike their results, however, the PDF tails do not overlap across Ra; instead, they broaden with increasing Ra. This indicates increased intermittency with increasing Ra.

Figure 8(c–d) presents the PDFs of the normal and shear components, respectively, at different heights for the highest $Ra = 4.8 \times 10^6$. The normal components show non-overlapping tails across heights, while the shear components largely collapse onto each other. Overall, grouping into normal and shear components reveals stronger intermittency than analysing the individual gradient components, as evidenced by the deviations of the tails from a Gaussian reference. Also, the PDF tails of both the normal and shear components follow the exponential distribution for various heights.

Figure 9 shows the skewness and flatness values at various heights in the bottom half of the cell for three different Ra. This further summarises the trends, which were displayed in figures 6 and 7. Panels (a) and (b) show the skewness values for normal and shear components, respectively. The normal components in the bulk are more skewed than near the plate, where they are nearly symmetric. The shear components are approximately symmetric and become slightly skewed with increasing Ra. In the bulk, the shear components remain near symmetric, while the normal components are skewed, consistent with the results of Xu *et al.* (2024). However, the skewness of their shear components

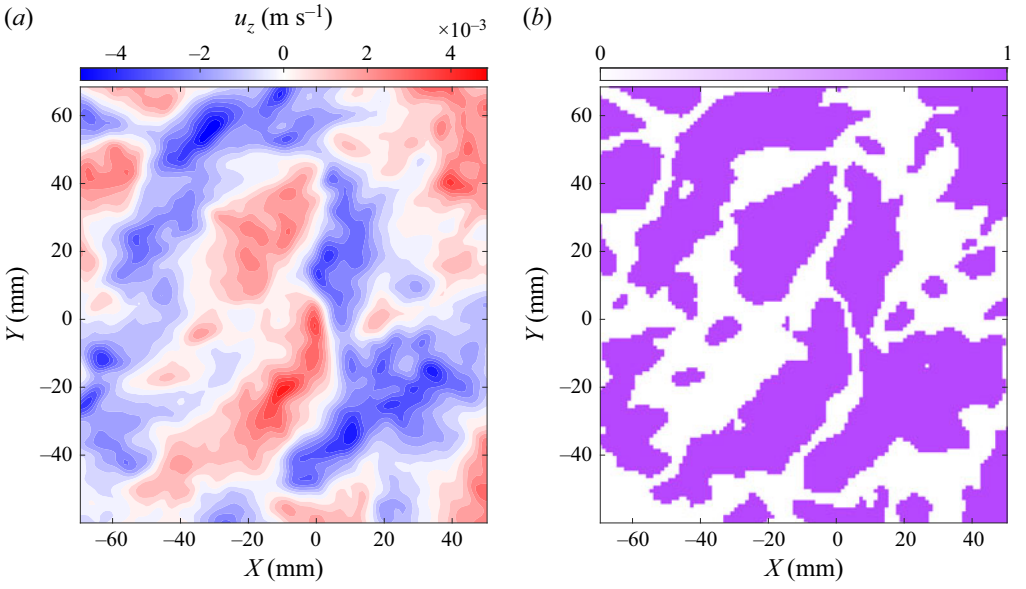

Figure 10. (*a*) Time-averaged field of vertical velocity revealing superstructure at mid-height for $Ra = 4.8 \times 10^6$. The averaging time is approximately $30T_f$ (200 snapshots). (*b*) Corresponding binary classification of vertical velocity regions at mid-height for $\alpha = 0.2$. Near-zero regions are shown in white, while regions with significant vertical velocity are shown in purple.

reaches values close to -0.5, which may be attributed to the fully turbulent flow at higher Ra, whereas our analysis reflects the influence of a transient regime.

Panels (*c*) and (*d*) of figure 9 show the flatness values for the normal and shear components, respectively. Here, both the normal and shear components take flatness values above the Gaussian value, as indicated by the dashed line. Similar to Xu *et al.* (2024), the shear components exhibit higher flatness values than the normal components, and the flatness increases with increasing Ra. In general, region near the bottom plate appears somewhat more intermittent than those in the bulk.

3.2.4. *Conditional statistics of upwelling and downwelling regions*

Further, to investigate the origin of the differences in the small-scale statistics of the velocity gradients between high-aspect-ratio and unity-aspect-ratio cells, we first performed a conditional analysis using the experimental data. This analysis focuses on separating regions corresponding to significant upwelling or downwelling from near-zero vertical velocity zones. Eliminating the near-zero regions allows statistical analysis to be performed in the regions of significant upwelling or downwelling, similar to those observed in unity-aspect-ratio cells.

Figure 10(*a*) shows the mid-height flow structure for $Ra = 4.8 \times 10^6$, obtained by averaging vertical velocity fields over thirty free-fall times. Upwelling, downwelling and near-zero vertical velocity regions are indicated in red, blue and white, respectively. In unity–aspect-ratio cells, a single LSC produces a mid-plane dominated entirely by upwelling or downwelling flow. In contrast, the high–aspect-ratio case exhibits multiple circulation rolls, giving rise to alternating bands of red and blue, separated by narrow white zones of weak vertical motion. To compare the two geometries, we compute conditional statistics of velocity gradients at mid-height, considering only the active upwelling and downwelling regions and excluding the near-zero zones that occupy the interfaces between them.

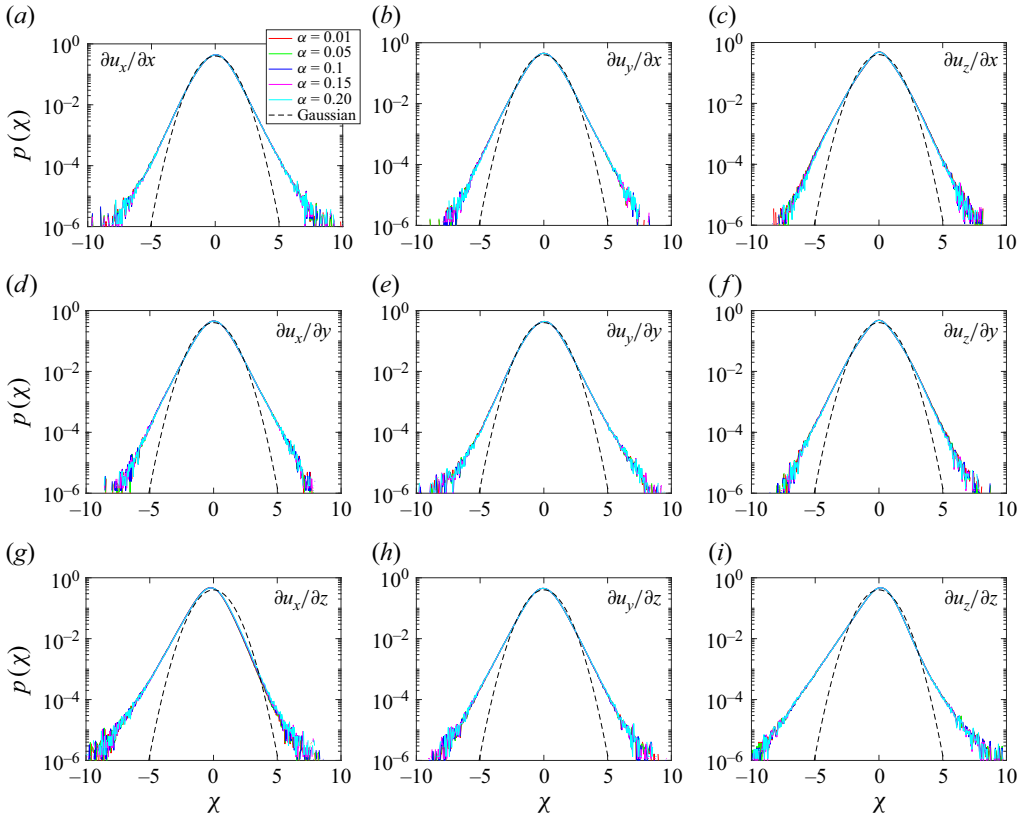

Figure 11. Conditional statistics of the nine velocity gradient tensor components at the mid-plane for $Ra = 4.8 \times 10^6$ and $Pr = 5$, shown for values of the threshold $\alpha = 0.01$, 0.05, 0.1, 0.15 and 0.2. The quantities shown are $\partial u_x/\partial x$ in (*a*), $\partial u_y/\partial x$ in (*b*), $\partial u_z/\partial x$ in (*c*), $\partial u_x/\partial y$ in (*d*), $\partial u_y/\partial y$ in (*e*), $\partial u_z/\partial y$ in (*f*), $\partial u_x/\partial z$ in (*g*), $\partial u_y/\partial z$ in (*h*), $\partial u_z/\partial z$ in (*i*), ω_x in (*j*), ω_y in (*k*) and ω_z in (*l*). All quantities are normalised by their respective root-mean-square values.

These regions are identified using a threshold based on the absolute magnitude of the vertical velocity

$$u_{z,th} = \alpha \times \max\left(|u_z(A, t)|\right), \tag{3.4}$$

where $u_z(A, t)$ denotes the vertical velocity over the horizontal area and over thirty free-fall times, and α is a free parameter. Regions where the absolute magnitude of the vertical velocity falls below this threshold correspond to near-zero zones, similar to the white regions shown in figure 10(*b*). The parameter α is varied between 0.01 and 0.2, which corresponds on average to 10 % and 47 % coverage of the total area, respectively. The remaining regions are considered for the conditional statistics. Similarly, we performed a sliding average of the vertical velocity (over $30T_f$) for each snapshot and used the chosen thresholds to separate the significant upwelling–downwelling regions from the near-zero regions. Once the regions of significant upwelling and downwelling are extracted for each snapshot, conditional statistics of the various velocity gradients can be performed within those regions.

Figure 11 shows the conditional statistics of all nine velocity gradients for five different values of $\alpha = 0.01$, 0.05, 0.1, 0.15 and 0.2. As α increases, more regions with near-zero vertical velocity are eliminated, and consequently, progressively smaller areas are

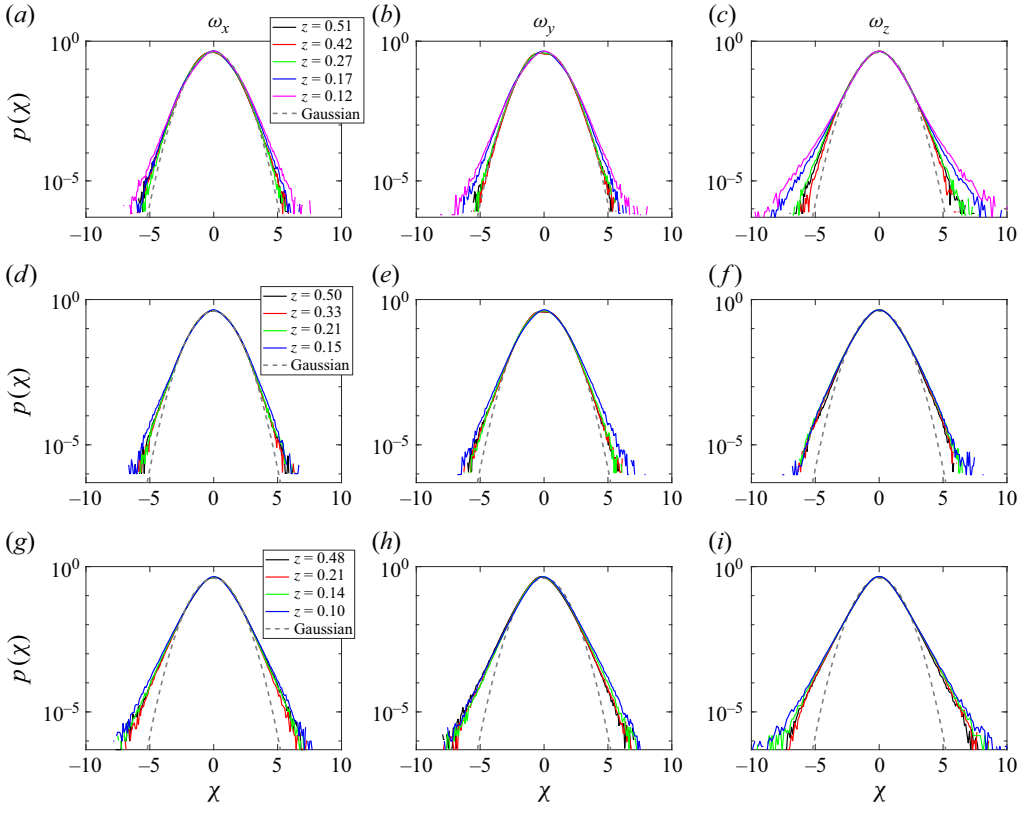

Figure 12. Probability density functions of vorticity components for four different planes in the z-direction at $Ra = 3.7 \times 10^5$ in (*a–c*), $Ra = 9.9 \times 10^5$ in (*d–f*) and $Ra = 4.8 \times 10^6$ in (*g–i*). The quantities shown are ω_x in (*a*,*d*,*g*), ω_y in (*b*,*e*,*h*) and ω_z in (*c*,*f*,*i*). In (*a–c*): $z = 0.51$ (black), $z = 0.42$ (red), $z = 0.27$ (green), $z = 0.17$ (blue), $z = 0.12$ (magenta), Gaussian (dashed, grey). In (*d–f*): $z = 0.50$ (black), $z = 0.33$ (red), $z = 0.21$ (green), $z = 0.15$ (blue), Gaussian (dashed, grey). In (*g–i*): $z = 0.48$ (black), $z = 0.21$ (red), $z = 0.14$ (green), $z = 0.10$ (blue), Gaussian reference (dashed, grey).

considered for the conditional statistics. Even though the area included in the analysis significantly decreases as α increases from 0.01 to 0.2, the PDFs of the velocity gradients largely overlap. This independence of the derivative statistics on the free parameter α may be due to the velocity gradients being small at these Ra. Similar trends were observed at other Ra values considered in the experiments. In addition, DNS data at $Ra = 1 \times 10^6$ and $Pr = 6.6$, with a spatial resolution of 2500×2500 and a temporal resolution of 0.1 over 300 free-fall time units (not shown), also indicate that the PDFs of the velocity gradients are largely insensitive to the values of α. The results do not yet allow us to determine the origin of differences between small-scale statistics of velocity gradients between high-aspect-ratio and unity-aspect-ratio cells. This is possibly because the velocity gradients in the current analysis are smaller at these low Ra. Extending the present analysis to higher $Ra \approx 10^8$ and $\Gamma \geqslant 8$ cell would provide a more comprehensive understanding.

3.2.5. *Vorticity components*

Figure 12 shows the PDFs of the vorticity components ω_x, ω_y and ω_z at multiple x-y planes in the bottom half of the convection cell for three different Ra values: $Ra =$

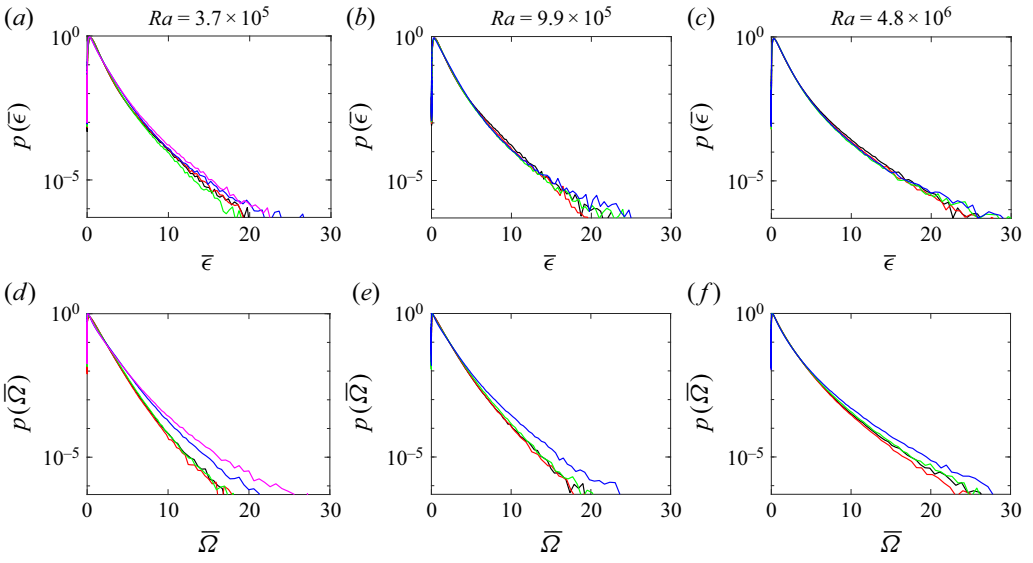

Figure 13. Probability density functions of normalised kinetic energy dissipation rate (top row) and local enstrophy (bottom row) at multiple planes in the z-direction at $Ra = 3.7 \times 10^5$ in (a,d), $Ra = 9.9 \times 10^5$ in (b,e) and $Ra = 4.8 \times 10^6$ in (c,f). Notations at the x axes are $\overline{\epsilon} = \epsilon/\langle\epsilon\rangle_{A,t}$ and $\overline{\Omega} = \Omega/\langle\Omega\rangle_{A,t}$. The heights of planes in the z-direction are indicated in same way as that in figure 12. In (a,d) $z = 0.51$ (black), $z = 0.42$ (red), $z = 0.27$ (green), $z = 0.17$ (blue), $z = 0.12$ (magenta). In (b,e) $z = 0.50$ (black), $z = 0.33$ (red), $z = 0.21$ (green), $z = 0.15$ (blue). In (c,f) $z = 0.48$ (black), $z = 0.21$ (red), $z = 0.14$ (green), $z = 0.10$ (blue).

3.7×10^5, 9.9×10^5 and 4.8×10^6. Recall that the dimensionless values z/δ_T for these x-y-planes are listed in table 2. Previous observations from the PDFs of vorticities at the mid-height in figure 4 demonstrated that intermittency increases with increasing Ra. A similar trend is observed for the PDFs of ω_x, ω_y and ω_z in figure 12, where the tails become somewhat fatter with increasing Ra. Figure 12 shows furthermore that the tails of the PDFs, for instance of ω_x, widen as we move closer to the heating plate. This suggests enhanced intermittency near the plate compared with the bulk. The trend holds for all vorticity components, ω_x, ω_y and ω_z, across the three Ra values. The increased intermittency near the wall is likely caused by turbulent plumes detaching from the boundary layers. This can proceed in the form of swirling motion.

3.3. *Statistics of energy dissipation and local enstrophy*

Figure 13 shows PDFs of the normalised kinetic energy dissipation rate and local enstrophy at multiple x-y planes in the bottom half of the convection cell, again for three different values $Ra = 3.7 \times 10^5$, 9.9×10^5 and 4.8×10^6. The heights of these planes are the same as those in figure 12. A comparison of the right tails of the dissipation and local enstrophy PDFs confirms that intermittency intensifies with increasing Ra. Next, we examine the right tails of the dissipation and enstrophy PDFs at mid-height and three additional planes located at the same heights z/δ_T, such that they are comparable. These data are represented by exactly the same line style as that shown in the legend of figure 12. Since plumes are result of boundary layer instabilities, non-dimensionalising the measurement plane heights using the characteristic thermal boundary layer thickness provides a more natural and appropriate choice to analyse enhanced intermittency in the proximity of the plates. Further, a recent study has shown that plume coalescence predominantly occurs near the plates and contributes to the formation of large-scale structures (Shevkar

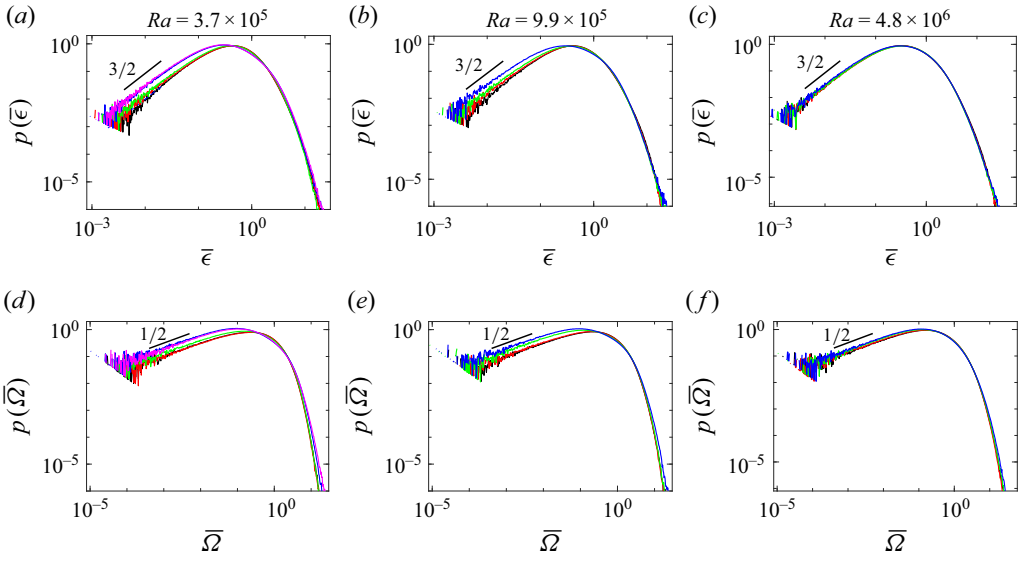

Figure 14. Figures are same as those in figure 13 except both x and y axes are in logarithmic units. In (a,d) $z = 0.51$ (black), $z = 0.42$ (red), $z = 0.27$ (green), $z = 0.17$ (blue), $z = 0.12$ (magenta). In (b,e) $z = 0.50$ (black), $z = 0.33$ (red), $z = 0.21$ (green), $z = 0.15$ (blue). In (c,f) $z = 0.48$ (black), $z = 0.21$ (red), $z = 0.14$ (green), $z = 0.10$ (blue). Notation agrees with figure 13.

et al. 2025*b*). This behaviour of enhanced intermittency in the proximity to the plate is further reflected in the PDFs of dissipation and local enstrophy. The tails extend to higher values of dissipation and local enstrophy as the planes approach the bottom plate, indicating increased intermittency near the plate. Additionally, for $Ra = 3.7 \times 10^5$, we include magenta curves in the plots, representing the plane closest to the bottom plate. This further reinforces the idea that intermittency increases as we move closer to the bottom plate. This behaviour follows the trend observed in the vorticity PDFs, which also show increased intermittency as we approach the bottom plate.

In figure 14, we replot the data of figure 13, but on a doubly logarithmic scale, to examine the left-tail behaviour. Interestingly, we observe a clear power law scaling for the left tail, with a 3/2 slope for the dissipation and a 1/2 slope for the enstrophy. This provides experimental confirmation of the left-tail scaling trends in convection which were previously suggested by Gotoh & Yang (2022) for HIT. The scaling thus remains valid for a large range of Reynolds numbers in different turbulent flows. At very low Reynolds numbers, the flow is mostly smooth and locally laminar, characterised by low strain rates and small-amplitude velocity gradients. In this regime, quantities such as the dissipation rate and local enstrophy follow approximately Gaussian statistics. Importantly, similar low-amplitude regions also exist as part of the background field in fully developed turbulent flows – i.e. in spatial domains where the normalised dissipation $\varepsilon/\langle\varepsilon\rangle_{A,t} \ll 1$ or the enstrophy $\Omega/\langle\Omega\rangle_{A,t} \ll 1$. In these regions, the flow remains nearly linear and Gaussian-like, and does not participate significantly in the nonlinear energy cascade. In such regions, PDFs of the dissipation and local enstrophy show the tail scalings of 3/2 and 1/2, respectively. The probability of left-tail events of the dissipation or enstrophy is generally higher for the near-wall regions compared with the bulk. As Ra increases, the tails of energy dissipation and local enstrophy at different heights approach each other, but convergence is not yet evident within the current Ra range. Further, we plot the kinetic energy dissipation and enstrophy values for various heights at three different

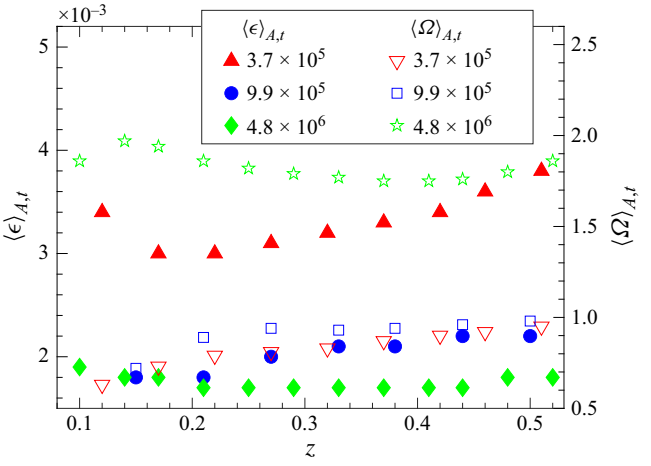

Figure 15. Mean kinetic energy dissipation rate and enstrophy at multiple z-planes in the bottom half of the convection cell for three different Ra.

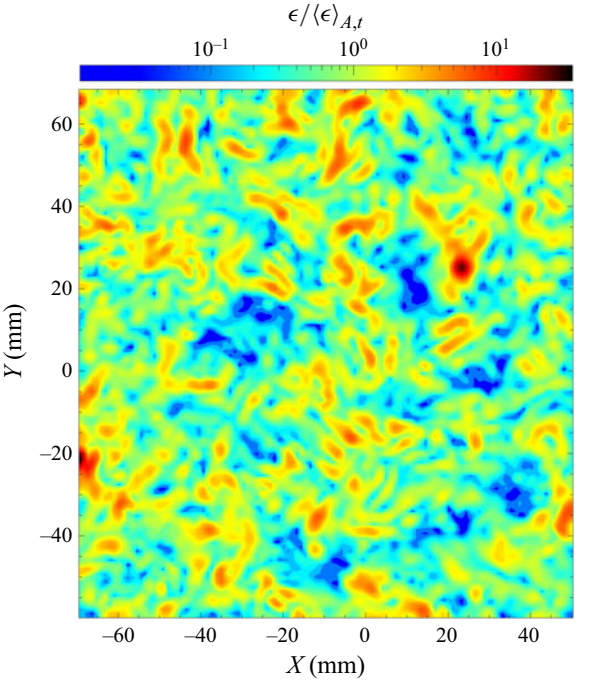

Figure 16. Instantaneous distribution of the normalised kinetic energy dissipation at a mid-plane for $Ra = 4.8 \times 10^6$.

Ra, shown in figure 15. At any specific height, the spatio-temporally averaged values of dissipation decrease with an increase in Ra, while those of enstrophy increase. The values of dissipation and local enstrophy are found to remain almost constant in the bulk of the convection cell. We also list the kinetic energy dissipation and enstrophy values in Appendix C.

Figure 16 shows the instantaneous distribution of the normalised kinetic energy dissipation at the mid-plane for $Ra = 4.8 \times 10^6$. The colour scale is plotted in logarithmic units.

The figure reveals a broad range of dissipation values contributing to both the left and right tails of the dissipation PDF. Blue regions indicate widespread, low-dissipation areas where the flow is nearly uniform in the horizontal plane, with small velocity gradients. A small, isolated black region at $(X, Y) = (23, 25)$ mm marks a localised, intermittent high-dissipation spot indicative of an extreme or high-amplitude event.

4. Conclusions and outlook

We presented results on the statistics of components of the velocity gradient tensor from spatio-temporally resolved 3-D velocity fields in RBC experiments. These experiments were conducted in a cell with square cross-section with an aspect ratio of $\Gamma = L/H = 25$, a laboratory set-up of mesoscale convection. The results were presented at mid-height and multiple planes in the bottom half of the convection cell. They covered parameter ranges $3.7 \times 10^5 \leqslant Ra \leqslant 4.8 \times 10^6$ and $5 \leqslant Pr \leqslant 7.1$.

Moderately dense particle images ($\sim$0.01 particles per pixel) were recorded using four sCMOS cameras. The particle images were further processed using the Lagrangian particle tracking velocimetry algorithm known as *STB*, available in the software package DaVis 10.2. The resulting particle positions, velocities and accelerations were then processed to obtain complete 3-D Eulerian velocity fields using VIC#. The final spatial resolution of velocity fields is of the order of the Kolmogorov length scale. At mid-height, all nine components of the velocity gradient tensor, as well as the components of vorticity obtained from one series of the experiments, were in good agreement with the ones from DNS at the same $Ra = 1 \times 10^6$ and $Pr = 6.6$. Along with this, the statistical convergence of derivative moments up to sixth order supports the reliability of the far-tail gradient events and the accuracy of the experimental data reported in the present study.

Our investigation focuses on derivative statistics. To this end, we examined the high-amplitude events or tails of the PDFs of all nine components of the velocity gradient tensor, three vorticity components, kinetic energy dissipation and local enstrophy in four planes located in the bottom half of the convection cell. The planes at three different Ra, other than the one at the mid-height, were chosen such that their normalised vertical location, z/δ_T, was the same. This choice enabled a direct comparison of planes located at the same normalised height for different Ra values. The tails of the PDFs of the derivatives become increasingly wide with increasing Ra, consistent with Schumacher *et al.* (2014). This was further confirmed by the systematic increase in flatness values with increasing Ra at all heights in the bottom half of the convection cell. Additionally, the tails also widen as one moves from the bulk region toward the bottom plate, for the range of Ra in the present study. This clearly indicates that intermittency increases both with increasing Ra and with closer proximity to the plates, compared with the bulk. In general, the estimated skewness values and the shapes of the PDFs of higher-order moments of the velocity gradients indicated that the vertical velocity derivatives are more skewed compared with the horizontal ones which might be caused by the thermal plumes that plunge into the central region of the layer.

In the bulk, the tails of the PDFs of velocity gradients follow an exponential distribution, similar to Xu *et al.* (2024). For direct comparison, we grouped the velocity gradients into normal and shear components. However, unlike their results, the PDF tails of both the normal and shear components widen with increasing Ra, indicating enhanced intermittency.

Conditional statistics, computed by excluding near-zero vertical velocity regions, indicate that the PDFs of velocity gradients remain largely unchanged across thresholds and Ra. This reflects the relatively small gradients at the lower Ra considered. Higher

Ra and larger-aspect-ratio domains will be required to fully resolve differences with unity-aspect-ratio cells.

Similarly, we also analysed the left tails of the kinetic energy dissipation and local enstrophy at four planes in the bottom half of the convection cell for $Ra = 3.7 \times 10^5$, 9.9×10^5 and 4.8×10^6. The left tails display slopes of $3/2$ and $1/2$ at all heights for the kinetic energy dissipation and local enstrophy, respectively. These observed slopes are the experimental confirmation of the highly resolved DNS results by Gotoh & Yang (2022) for HIT. Furthermore, in general, these tails exhibited higher probabilities with increasing proximity to the plate, in comparison with the bulk. In the present study, the area-time-averaged values of the energy dissipation and local enstrophy remained nearly constant in the bulk of the convection cell. To summarise, with our reported laboratory experiments we were able to analyse the full 3-D small-scale structure of the velocity field in different heights of an RBC layer.

In the future, we plan to extend the analysis by exploring higher Rayleigh numbers up to $Ra \sim 10^8$. This requires a reduction of the cell aspect ratio to $\Gamma = 10$. This work, together with Lagrangian dispersion studies in mesoscale RBC, is currently underway and will be reported elsewhere. A further aspect is to combine these volumetric analyses with the temperature field, which can be done for example by a combination with physics-informed machine learning techniques, such as in Toscano *et al.* (2025), or using direct measurements as in Käufer & Cierpka (2024).

Acknowledgements. Authors would like to thank A. Thieme for the support with the experiments.

Funding. The research of P.P.S. and R.J.S. is funded by the European Union (ERC, MesoComp, 101052786). Views and opinions expressed are, however, those of the authors only and do not necessarily reflect those of the European Union or the European Research Council.

Declaration of interests. The authors report no conflict of interest.

Data availability statement. The dataset and scripts for reproducing the figures presented in present work are available on Zenodo (Shevkar *et al.* 2025*a*).

Appendix A. Direct numerical simulations

In this appendix, we describe the DNS used for comparison with experiments. They solve the 3-D Navier–Stokes equations with Boussinesq coupling of the velocity $\boldsymbol{u}(\boldsymbol{x}, t) = (u_x, u_y, u_z)$ and temperature $T(\boldsymbol{x}, t)$ fields (Verma 2018). The dimensionless form of the governing equations is given by

$$\frac{\partial \boldsymbol{u}}{\partial t} + (\boldsymbol{u} \cdot \boldsymbol{\nabla})\boldsymbol{u} = -\boldsymbol{\nabla} p + T\hat{\boldsymbol{z}} + \sqrt{\frac{Pr}{Ra}}\,\nabla^2 \boldsymbol{u}, \tag{A1}$$

$$\frac{\partial T}{\partial t} + (\boldsymbol{u} \cdot \boldsymbol{\nabla})T = \frac{1}{\sqrt{PrRa}}\,\nabla^2 T, \tag{A2}$$

$$\boldsymbol{\nabla} \cdot \boldsymbol{u} = 0. \tag{A3}$$

The equations are solved by the spectral element method (SEM) using the GPU accelerated SEM solver, nekRS (Fischer *et al.* 2022). While the experiments were conducted in a closed cell with aspect ratio $\Gamma = 25$, we choose our computational domain to be a cuboidal cell of $\Gamma = 8$, but with periodic boundary conditions in the horizontal directions. The top and bottom walls enforce no-slip condition on the velocity field and are isothermally maintained at $T_c = 0$ and $T_h = 1$, respectively. This DNS configuration approximates the inner region of the experimental cell well.

We follow the same workflow as in Samuel *et al.* (2024). Consequently, we ensure that the meshes are fine enough to resolve the boundary layers, and the simulations are

Ra	Pr	Γ	N_{pts}	T_f	Nu	Re
3.7×10^5	7.1	8	$1750 \times 1750 \times 448$	2750	6.23 ± 0.10	22.4 ± 0.2
1.0×10^6	6.6	8	$1750 \times 1750 \times 448$	2350	8.49 ± 0.11	41.7 ± 0.6

Table 4. Details of the DNS. Listed here are the Rayleigh number, Ra, Prandtl number, Pr, the aspect ratio, Γ, the number of collocation points along the x-, y- and z-directions, N_{pts}, the total averaging time in free-fall units, T_f, the time-averaged Nusselt number at the walls, Nu, and the Reynolds number, Re. Mean values in the last two columns are accompanied by their standard deviations.

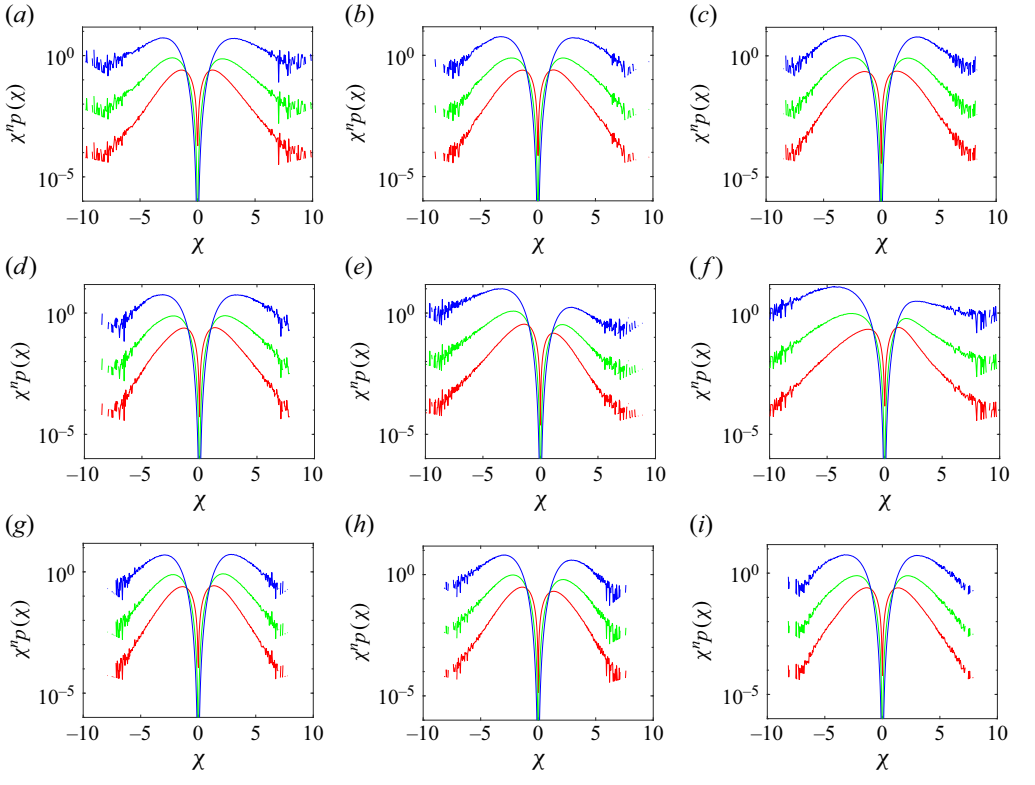

Figure 17. Statistical convergence of higher-order velocity derivative statistics for the experiments at the mid-height $z = 0.5$ for $Ra = 4.8 \times 10^6$ and $Pr = 5.0$. The quantities shown are $\partial u_x/\partial x$ in (a), $\partial u_y/\partial x$ in (b), $\partial u_z/\partial x$ in (c), $\partial u_x/\partial y$ in (d), $\partial u_x/\partial z$ in (e), $\partial u_z/\partial z$ in (f), ω_x in (g), ω_y in (h) and ω_z in (i). All quantities are normalised by their respective r.m.s. values. Here, $n = 2$, 4 and 6 for red, green and blue solid lines, respectively. Note that the y-axis is in logarithmic units.

run long enough to get reliable statistics for a statistically steady state. The pertinent details of the simulations are listed in table 4. The table also lists the numerically computed Nusselt number, Nu, and Reynolds number, Re, which are the global measures of heat transport and momentum transport, respectively. We compute Nu from the non-dimensionalised temperature gradient at the bottom wall, whereas Re is calculated from the volume-averaged root-mean-square (r.m.s.) velocity, see also (1.3)

$$Nu = -\left.\frac{\partial \langle T \rangle_{A,t}}{\partial z}\right|_{z=0}, \qquad Re = U_{rms}\sqrt{\frac{Ra}{Pr}}. \tag{A4}$$

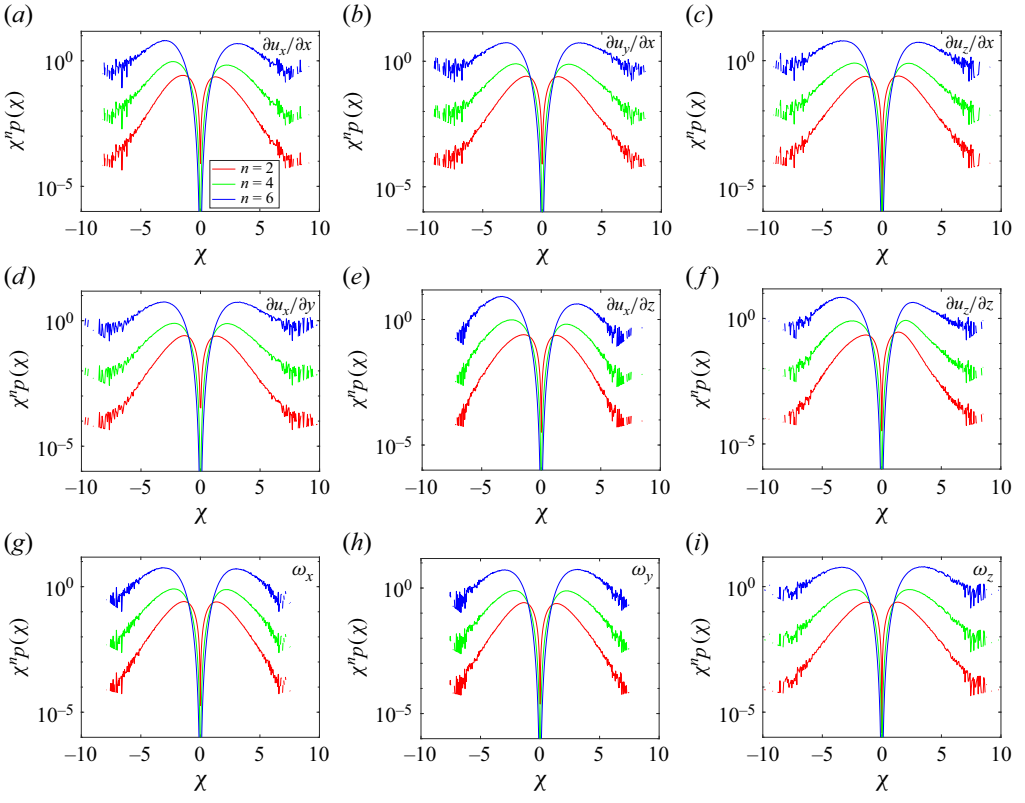

Figure 18. Statistical convergence of higher-order velocity derivative statistics for the experiments at $z = 0.1$ for $Ra = 4.8 \times 10^6$ and $Pr = 5.0$. The quantities shown are $\partial u_x/\partial x$ in (*a*), $\partial u_y/\partial x$ in (*b*), $\partial u_z/\partial x$ in (*c*), $\partial u_x/\partial y$ in (*d*), $\partial u_x/\partial z$ in (*e*), $\partial u_z/\partial z$ in (*f*), ω_x in (*g*), ω_y in (*h*) and ω_z in (*i*). All quantities are normalised by their respective r.m.s. values. Here, $n = 2$, 4 and 6 for red, green and blue solid lines, respectively. Note that the y-axis is in logarithmic units.

The r.m.s. velocity is computed as $U_{rms} = \langle \boldsymbol{u}^2 \rangle_{V,t}^{1/2}$. The standard deviations of *Nu* and *Re* are computed from their respective time series and displayed as the measurement uncertainty for each of them in the table.

Appendix B. Statistical convergence of derivative moments at $Ra = 4.8 \times 10^6$

The statistical convergence of the selected velocity derivative and all three vorticity components at the highest $Ra = 4.8 \times 10^6$ at the mid-height is here demonstrated in figure 17. Here, $n = 2$, 4 and 6 stand for the red, green and blue solid lines in the panels, respectively. The good convergence of the displayed components indicates that the tails tend to decay toward zero. This is definitely obtained for $n = 2$, 4; a decay is, however, also observable for $n = 6$. Thus, we conclude a convergence up to derivative moment order $n = 6$. The higher-order derivative statistics clearly showcase that the $\partial u_x/\partial z$ and $\partial u_z/\partial z$ profiles are more skewed compared with the other velocity derivatives in the x- and y-directions. Similar observations are valid for other three derivative components which are not shown here. This finding also agrees with the numerical and experimental results for RBC in air by Valori & Schumacher (2021) and Valori *et al.* (2022), respectively. We also checked for statistical convergence of the data near the plate and observed good convergence, as shown in figure 18.

$Ra = 3.7 \times 10^5$			$Ra = 9.9 \times 10^5$			$Ra = 4.8 \times 10^6$		
z	$\langle\epsilon\rangle_{A,t}$	$\langle\Omega\rangle_{A,t}$	z	$\langle\epsilon\rangle_{A,t}$	$\langle\Omega\rangle_{A,t}$	z	$\langle\epsilon\rangle_{A,t}$	$\langle\Omega\rangle_{A,t}$
0.51	3.8×10^{-3}	0.95	0.50	2.2×10^{-3}	0.98	0.52	1.8×10^{-3}	1.86
0.46	3.6×10^{-3}	0.92	0.44	2.2×10^{-3}	0.96	0.48	1.8×10^{-3}	1.80
0.42	3.4×10^{-3}	0.90	0.38	2.1×10^{-3}	0.94	0.44	1.7×10^{-3}	1.76
0.37	3.3×10^{-3}	0.87	0.33	2.1×10^{-3}	0.93	0.41	1.7×10^{-3}	1.75
0.32	3.2×10^{-3}	0.83	0.27	2.0×10^{-3}	0.94	0.37	1.7×10^{-3}	1.75
0.27	3.1×10^{-3}	0.81	0.21	1.8×10^{-3}	0.89	0.33	1.7×10^{-3}	1.77
0.22	3.0×10^{-3}	0.79	0.15	1.8×10^{-3}	0.72	0.29	1.7×10^{-3}	1.79
0.17	3.0×10^{-3}	0.73				0.25	1.7×10^{-3}	1.82
0.12	3.4×10^{-3}	0.63				0.21	1.7×10^{-3}	1.86
						0.17	1.8×10^{-3}	1.94
						0.14	1.8×10^{-3}	1.97
						0.10	1.9×10^{-3}	1.86

Table 5. Mean kinetic energy dissipation rate and enstrophy at multiple z-planes in the bottom half of the convection cell for three different Ra.

Appendix C. Mean values of the dissipation and local enstrophy

We list the kinetic energy dissipation and enstrophy values for various heights at three different Ra in table 5. Values are the same as those plotted in figure 15.

References

Ahlers, G., Grossmann, S. & Lohse, D. 2009 Heat transfer and large scale dynamics in turbulent Rayleigh–Bénard convection. *Rev. Mod. Phys.* **81**, 503–537.

Alam, S., Krasnov, D., Pandey, A., Panickacheril John, J., Samuel, R.J., Vieweg, P.P. & Schumacher, J. 2025 Turbulent mesoscale convection in the Boussinesq limit and beyond. *Intl J. Heat Fluid Flow* **115**, 109856.

Atkinson, B.W. & Wu Zhang, J. 1996 Mesoscale shallow convection in the atmosphere. *Rev. Geophys.* **34** (4), 403–431.

Bailon-Cuba, J., Emran, M.S. & Schumacher, J. 2010 Aspect ratio dependence of heat transfer and large-scale flow in turbulent convection. *J. Fluid Mech.* **655**, 152–173.

Chen, H. & Chen, S. 1998 Kinematic effects on local energy dissipation rate and local enstrophy in fluid turbulence. *Phys. Fluids* **10** (1), 312–314.

Chen, S., Sreenivasan, K.R. & Nelkin, M. 1997 Inertial range scalings of dissipation and enstrophy in isotropic turbulence. *Phys. Rev. Lett.* **79**, 1253–1256.

Chong, M.S., Perry, A.E. & Cantwell, B.J. 1990 A general classification of three-dimensional flow fields. *Phys. Fluids* **2**, 765–777.

Donzis, D.A., Yeung, P.K. & Sreenivasan, K.R. 2008 Dissipation and enstrophy in isotropic turbulence: resolution effects and scaling in direct numerical simulations. *Phys. Fluids* **20** (4), 045108.

Ducci, A. & Yianneskis, M. 2005 Direct determination of energy dissipation in stirred vessels with two-point LDA. *AIChE J.* **51** (8), 2133–2149.

Emran, M.S. & Schumacher, J. 2008 Fine-scale statistics of temperature and its derivatives in convective turbulence. *J. Fluid Mech.* **611**, 13–34.

Emran, M.S. & Schumacher, J. 2012 Conditional statistics of thermal dissipation rate in turbulent Rayleigh–Bénard convection. *Eur. Phys. J. E* **35**, 9786.

Ettel, M., Vieweg, P.P. & Schumacher, J. 2025 Effects of conjugate heat transfer on large-scale flow structures in convection. *J. Fluid Mech.* **1016**, A30.

Fischer, P.F. *et al.* 2022 NekRS, a GPU-accelerated spectral element Navier–Stokes solver. *Parallel Comput.* **114**, 102982.

Ghazijahini, M.S. & Cierpka, C. 2024 Spatio-temporal dynamics of superstructures and vortices in turbulent Rayleigh–Bénard convection. *Phys. Fluids* **36**, 035120.

GOTOH, T., WATANABE, T. & SAITO, I. 2023 Kinematic effects on probability density functions of energy dissipation rate and enstrophy in turbulence. *Phys. Rev. Lett.* **130**, 254001.
GOTOH, T. & YANG, J. 2022 Transition of fluctuations from Gaussian state to turbulent state. *Phil. Trans. R. Soc. A* **380**, 20210097.
GROSSMANN, S. & LOHSE, D. 2000 Scaling in thermal convection: a unifying theory. *J. Fluid Mech.* **407**, 27–56.
INCROPERA, F.P. 1988 Convection heat transfer in electronic equipment cooling. *J. Heat Transfer* **110** (4b), 1097–1111.
JEON, Y., MÜLLER, M. & MICHAELIS, D. 2022 Fine scale reconstruction (VIC#) by implementing additional constraints and coarse-grid approximation into VIC+. *Exp. Fluids* **63**, 70.
KÄHLER, C.J., SCHARNOWSKI, S. & CIERPKA, C. 2012 On the resolution limit of digital particle image velocimetry. *Exp. Fluids* **52**, 1629–1639.
KÄUFER, T. & CIERPKA, C. 2024 Volumetric Lagrangian temperature and velocity measurements with thermochromic liquid crystals. *Meas. Sci. Technol.* **35**, 035301.
KÄUFER, T., VIEWEG, P.P., SCHUMACHER, J. & CIERPKA, C. 2023 Thermal boundary condition studies in large aspect ratio Rayleigh–Bénard convection. *Eur. J. Mech. B/Fluids* **101**, 283–293.
LIBERZON, A., GUALA, M., KINZELBACH, W. & TSINOBER, A. 2006 On turbulent kinetic energy production and dissipation in dilute polymer solutions. *Phys. Fluids* **18** (12), 125101.
LIBERZON, A., GURKA, R., SARATHI, P. & KOPP, G.A. 2012 Estimate of turbulent dissipation in a decaying grid turbulent flow. *Exp. Therm. Fluid Sci.* **39**, 71–78.
MOLLER, S., KÄUFER, T., PANDEY, A., SCHUMACHER, J. & CIERPKA, C. 2022 Combined particle image velocimetry and thermometry of turbulent superstructures in thermal convection. *J. Fluid Mech.* **945**, A22.
MOLLER, S., RESAGK, C. & CIERPKA, C. 2020 On the application of neural networks for temperature field measurements using thermochromic liquid crystals. *Exp. Fluids* **61**, 111.
MOLLER, S., RESAGK, C. & CIERPKA, C. 2021 Long-time experimental investigation of turbulent superstructures in Rayleigh–Bénard convection by noninvasive simultaneous measurements of temperature and velocity fields. *Exp. Fluids* **62**, 64.
NIEMELA, J.J., SKRBEK, L., SREENIVASAN, K.R. & DONELLY, R.J. 2001 The wind in confined thermal convection. *J. Fluid Mech.* **449**, 169–178.
PANDEY, A., SCHEEL, J.D., SCHUMACHER, P. & J 2018 Turbulent superstructures in Rayleigh–Bénard convection. *Nat. Commun.* **9**, 2118.
ROCKSTROH, T. & MICHAELIS, D. 2021 Uncertainty quantification for PTV/LPT data and adaptive track filtering. In *14th International Symposium on Particle Image Velocimetry*, pp. 1.
SAMUEL, R.J., BODE, M., SCHEEL, J.D., SREENIVASAN, K.R. & SCHUMACHER, J. 2024 No sustained mean velocity in the boundary region of plane thermal convection. *J. Fluid Mech.* **996**, A49.
SCHANZ, D., GESEMANN, S. & SCHRÖDER, A. 2016 Shake-the-box: Lagrangian particle tracking at high particle image densities. *Exp. Fluids* **57**, 70.
SCHANZ, D., GESEMANN, S., SCHRÖDER, A., WIENEKE, B. & NOVARA, M. 2012 Non-uniform optical transfer functions in particle imaging: calibration and application to tomographic reconstruction. *Meas. Sci. Technol.* **24**, 024009.
SCHEEL, J., EMRAN, S. & SCHUMACHER, J. 2013 Resolving the fine-scale structure in turbulent Rayleigh–Bénard convection. *New J. Phys.* **15**, 113063.
SCHUMACHER, J., GÖTZFRIED, P. & SCHEEL, J.D. 2015 Enhanced enstrophy generation for turbulent convection in low-Prandtl-number fluids. *Proc. Natl Acad. Sci. USA* **112** (31), 9530–9535.
SCHUMACHER, J., PANDEY, A., YAKHOT, V. & SREENIVASAN, K.R. 2018 Transition to turbulence scaling in Rayleigh–Bénard convection. *Phys. Rev. E* **98**, 033120.
SCHUMACHER, J., SCHEEL, J.D., KRASNOV, D., DONZIS, D.A., YAKHOT, V. & SREENIVASAN, K.R. 2014 Small-scale universality in fluid turbulence. *Proc. Natl Acad. Sci. USA* **111** (30), 10961–10965.
SCIACCHITANO, A., LECLAIRE, B. & SCHRÖDER, A. 2021 Main results of the first data assimilation challenge. In *14th International Symposium on Particle Image Velocimetry*, pp. 1.
SHANG, X.D., TONG, PR & XIA, K.Q. 2008 Scaling of the local convective heat flux in turbulent Rayleigh–Bénard convection. *Phys. Rev. Lett.* **100**, 244503.
SHEVKAR, P.P., GUNASEGARANE, G.S., MOHANAN, S.K. & PUTHENVEETTIL, B.A. 2019 Effect of shear on coherent structures in turbulent convection. *Phys. Rev. Fluids* **4**, 043502.
SHEVKAR, P.P., MOHANAN, S.K. & PUTHENVEETTIL, B.A. 2023 Effect of shear on local boundary layers in turbulent convection. *J. Fluid Mech.* **962**, A41.
SHEVKAR, P.P., SAMUEL, R.J., CIERPKA, C. & SCHUMACHER, J. 2025*a* Repository for three-dimensional velocity gradient statistics in a mesoscale convection laboratory experiment. Zenodo. https://doi.org/10.5281/zenodo.17473075.

SHEVKAR, P.P., SAMUEL, R.J., ZINCHENKO, G., BODE, M., SCHUMACHER, J. & SREENIVASAN, K.R. 2025*b* Hierarchical network of thermal plumes and their dynamics in turbulent Rayleigh–Bénard convection. *Proc. Natl Acad. Sci. USA* **122**, e2502972122.

SHEVKAR, P.P., VISHNU, R., MOHANAN, S.K., KOOTHUR, V., MATHUR, M. & PUTHENVEETTIL, B.A. 2022 On separating plumes from boundary layers in turbulent convection. *J. Fluid Mech.* **941**, A5.

STEVENS, R.J.A.M., BLASS, A., ZHU, X., VERZICCO, R. & LOHSE, D. 2018 Turbulent thermal superstructures in Rayleigh–Bénard convection. *Phys. Rev. Fluids* **3**, 041501.

TOKGOZ, S., ELSINGA, G., DELFOS, R. & WESTERWEEL, J. 2012 Spatial resolution and dissipation rate estimation in Taylor–Couette flow for tomographic PIV. *Exp. Fluids* **53**, 561–583.

TOSCANO, J.D., KÄUFER, T., WANG, Z., MAXEY, M., CIERPKA, C. & KARNIADAKIS, G.EM 2025 AIVT: inference of turbulent thermal convection from measured 3D velocity data by physics-informed Kolmogorov–Arnold networks. *Sci. Adv.* **11**, eads5236.

VALORI, V., KRÄUTER, R. & SCHUMACHER, J. 2022 Extreme vorticity events in turbulent Rayleigh–Bénard convection from stereoscopic measurements and reservoir computing. *Phys. Rev. Res.* **4**, 023180.

VALORI, V. & SCHUMACHER, J. 2021 Connecting boundary layer dynamics with extreme bulk dissipation events in Rayleigh–Bénard flow. *Europhys. Lett.* **134**, 34004.

VENUGOPAL, V., DE, A. & MISHRA, P. 2022 Statistics of thermal plumes and dissipation rates in turbulent Rayleigh–Bénard convection in a cubic cell. *Intl J. Heat Mass Transfer* **182**, 121995.

VERMA, M.K. 2018 *Physics of Buoyant Flows*.World Scientific.

VERZICCO, R. & CAMUSSI, R. 2003 Numerical experiments on strongly turbulent thermal convection in a slender cylindrical cell. *J. Fluid Mech.* **477**, 19–49.

VIEWEG, P.P., KÄUFER, T., CIERPKA, C. & SCHUMACHER, J. 2025 Digital twin of a large-aspect-ratio Rayleigh–Bénard experiment: role of thermal boundary conditions, measurement errors and uncertainties. *Flow* **5**, E4.

VIEWEG, P.P., SCHEEL, J.D. & SCHUMACHER, J. 2021 Supergranule aggregation for constant heat flux-driven turbulent convection. *Phys. Rev. Res.* **3**, 013231.

VOROBEV, A., ZIKANOV, O., DAVIDSON, P.A. & KNAEPEN, B. 2005 Anisotropy of magnetohydrodynamic turbulence at low magnetic Reynolds number. *Phys. Fluids* **17** (12), 125105.

WAGNER, S. & SHISHKINA, O. 2013 Aspect-ratio dependency of Rayleigh–Bénard convection in box-shaped containers. *Phys. Fluids* **25** (8), 085110.

WALLACE, J.M. & VUKOSLAVČEVIĆ, P.V. 2010 Measurement of the velocity gradient tensor in turbulent flows. *Annu. Rev. Fluid Mech.* **42**, 157–181.

WANG, G., YANG, F., WU, K., MA, Y., PENG, C., LIU, T. & WANG, L. 2021 Estimation of the dissipation rate of turbulent kinetic energy: a review. *Chem. Engng Sci.* **229**, 116133.

WANG, H., LIU, Y. & WANG, S. 2022 Dense velocity reconstruction from particle image velocimetry/particle tracking velocimetry using a physics-informed neural network. *Phys. Fluids* **34**, 017116.

WEISS, S., SCHANZ, D., ERDOGDU, A., SCHRÖDER, A. & BOSBACH, J. 2023 Investigation of turbulent superstructures in Rayleigh–Bénard convection by Lagrangian particle tracking of fluorescent microspheres. *Exp. Fluids* **64**, 82.

WIENEKE, B. 2008 Volume self-calibration for 3D particle image velocimetry. *Exp. Fluids* **45**, 549–556.

XU, F., ZHANG, L. & XIA, K. 2024 Experimental measurement of spatio-temporally resolved energy dissipation rate in turbulent Rayleigh–Bénard convection. *J. Fluid Mech.* **984**, A8.

YEUNG, P.K., ZHAI, X.M. & SREENIVASAN, K.R. 2015 Extreme events in computational turbulence. *Proc. Natl Acad. Sci. USA* **112** (41), 12633–12638.

ZHANG, Y., ZHOU, Q. & SUN, C. 2017 Statistics of kinetic and thermal energy dissipation rates in two-dimensional turbulent Rayleigh–Bénard convection. *J. Fluid Mech.* **814**, 165–184.